Influence of Black Hole kicks on Gravitational Wave Ringdown

A Thesis

submitted to
Indian Institute of Science Education and Research Pune
in partial fulfillment of the requirements for the
BS-MS Dual Degree Programme

by

Harshal Nitin Chaware

Indian Institute of Science Education and Research Pune
Dr. Homi Bhabha Road,
Pashan, Pune 411008, INDIA.

May, 2026

Supervisor: Dr. Shilpa Kastha

Certificate

This is to certify that this dissertation entitled **Influence of Black Hole kicks on Gravitational Wave Ringdown** towards the partial fulfilment of the BS-MS dual degree programme at the Indian Institute of Science Education and Research, Pune represents study/work carried out by Harshal Nitin Chaware at the Indian Institute of Science Education and Research, Pune under the supervision of Dr. Shilpa Kastha, Associate Professor, Theory Division, Saha Institute of Nuclear Physics (SINP), Kolkata during the academic year 2025-2026.

Dr. Shilpa Kastha

Committee:
Dr. Shilpa Kastha
Dr. Susmita Adhikari

This thesis is dedicated to my parents.

Declaration

I hereby declare that the matter embodied in the report entitled **Influence of Black Hole kicks on Gravitational Wave Ringdown** are the results of the work carried out by me at the Department of Physics, Indian Institute of Science Education and Research (IISER), Pune and Saha Institute of Nuclear Physics (SINP), Kolkata under the supervision of Dr. Shilpa Kastha, Saha Institute of Nuclear Physics (SINP), Kolkata and have not been submitted elsewhere for any other degree. Wherever others contribute, every effort is made to indicate this clearly, with due reference to the literature and acknowledgement of collaborative research and discussions.

Harshal Nitin Chaware
Roll number: 20211248

Acknowledgements

I would like to thank Prof. Shilpa Kastha for offering me a position at SINP to conduct my Master's thesis with her. I am grateful for her patience in guiding me through the project. She gave me enough academic freedom which allowed to me explore several ideas on my own. I am also grateful to Dr. Akash Kumar Mishra for his valuable insights in the project and sharing his pipeline. I would like to acknowledge SINP for providing me accommodation and access to the institute facilities.

Throughout my stay at SINP, I met some amazing people without whom the year would have been dreadful. I would like to thank Aditya, Chitranshi, Deep, Hardey, Karan, Kartik, Parthajit, Priyanshu, Ritvik, Saheb, Shreyas, Soummyadip, and Utkarsh Bhaiyya. I am also grateful to some special people: Emanuel, Monalisa, Pugazhendi, Puja and Rajeswari. The time that I have spent with you will always be memorable.

The five years at IISER have been nothing short of a roller-coaster ride full of ups and downs. There are several things at IISER which have made my decision of pursuing my undergraduate here worthwhile. The most important of them are getting the freedom to choose the courses and connecting with amazing peers. Giving the academic freedom to choose the courses and let the student design the curriculum for himself/herself, in my opinion, is one of the best things an institute can offer. Unlike rigid academic structures which force the student to pursue a particular discipline–much like the blinders attached to a horse–IISER allowed me to explore different disciplines throughout the five year program.

As mentioned earlier, I came across a diverse set of people whom I would like to thank: Amlan, Amrutamshu, Anand Dubey, Anand Sharma, Anandh, Anirban, Anish, Anuraag, Atul, Authisha, Chitresh, Devesh, Eshwar, Goraksh, Heerak, Neeraj, Nikhil, Praneet, Prasad, Raghav, Rajat, Rakshaditya, Ritesh, Sarthak, Shubham Bhaiyya, Srujan, Sumiran, Sukshith, Sushant, Vatsal, Vishnu Kadam and Yash Gupta. I owe a special thanks to Anand Sharma, Anuraag, Devesh, Eshwar, Sukshith and Sushant for putting up with me and tolerating me in the last five years. Devesh, Eshwar and Sukshith have had the biggest impact on me and have changed the way I look at things.

I would also like to acknowledge the facilities provided by IISER to the students. I was amazed to see such wonderful hostel and sports facilities. Thanks to all the security, cleaning staff and gardening staff for maintaining these facilities well. I'll miss staying at 621 with all the (official and unofficial) roommates. I'll also miss playing badminton, basketball and football tournaments with my fellow teammates. I would also like to ac-

knowledge two student-run clubs at IISER whose events I enjoyed the most: Kaleidoscope and Spicmacay.

Finally, I would like to thank Aai and Baba for being the biggest support systems in my life. I fall short of words to express how grateful I am towards them and how much I love them. Whatever little I have achieved in life today, I owe it to them. Thanks Aai and Baba!

Abstract

Asymmetric emission of gravitational waves (GWs) during a binary black hole (BBH) merger leads to a recoil of the remnant black hole, commonly known as a black hole (BH) kick. The final stage of a BBH merger where the final BH which is in the perturbed state settles down by emitting gravitational radiation is known as ringdown. Using the linear black hole perturbation theory, ringdown is modeled as a linear superposition of damped sinusoids. Neglecting the effect of BH kicks in ringdown waveform models can introduce systematic biases in the inferred parameters. The recoil motion induces relativistic effects in the waveform, primarily Doppler shift and aberration: Doppler shift modifies the Quasi-normal mode frequencies, while aberration leads to mode mixing and affects the mode amplitudes. In this thesis, we investigate the systematic biases that arise when these effects are not incorporated in the ringdown model. Previous studies have primarily considered only the frequency shifts due to Doppler effects. Because the Doppler shift is degenerate with the remnant mass, neglecting this effect leads to biases in the estimated final mass. Aberration, on the other hand, introduces biases in the mode amplitudes and final spin through mode mixing. After incorporating these effects in the waveform model, we further study the prospects for detecting BH kicks using ringdown measurements alone. Due to the degeneracy between Doppler shift and the final mass, including only the Doppler effect does not allow an independent measurement of the kick, using only ringdown. We find that incorporating aberration does not significantly break this degeneracy, as the kick also couples to the mode amplitudes. Consequently, detecting kicks from ringdown observations alone remains challenging. Nevertheless, these effects must be accounted for to avoid systematic biases, particularly for future GW detectors where higher signal-to-noise ratios will make such biases more significant.

Contents

List of Tables

List of Figures

Chapter 1

Introduction

Shortly after proposing the General Theory of Relativity (GR) in 1915, Einstein predicted the existence of Gravitational Waves (GWs). The first indirect evidence for GWs came in 1974 with the discovery of the binary pulsar PSR B1913+16 by Russell Hulse and Joseph Taylor [1]. They observed that the orbit of the system was gradually shrinking at a rate in excellent agreement with the energy loss predicted by GR due to GW emission. However, the first direct detection of GWs occurred several decades later in 2015, when the twin LIGO [2] detectors in Hanford and Livingston observed the merger of two black holes (BHs) with masses of $36M_{\odot}$ and $29M_{\odot}$, located about 1.4 billion light-years from Earth [3]. So far, more than 200 compact binary mergers have been detected across the four observing runs of the GW detector network. [4, 5].

Gravitational Waves have opened an entirely new window of 'listening' to the Universe, offering unprecedented opportunities to explore fundamental physics, astrophysics, and cosmology. Over the last decade, signals from compact binary mergers have opened up various scientific avenues; some of them are testing GR in the strong field regime ([6] and references therein) , studying BH population properties [7–11] and learning about stellar progenitors [12–16]. Owing to the short duration of the signal and the limited sensitivity of the detector, several important aspects remain challenging to probe, which include GW memory effects ([17] and references therein) , post-merger dynamics beyond the linear order [18–25] and binaries with eccentric inspirals [26–30]. In 2025, the LIGO detectors recorded the event GW250114 which is the loudest recorded GW signal until now having a Signal-to-Noise Ratio (SNR) of 76 [31]. This event allowed us not only to perform a suite of tests spanning inspiral, merger and ringdown which constitute the most stringent single-event verification of GR, but also test Hawking's area law and Kerr nature of BHs

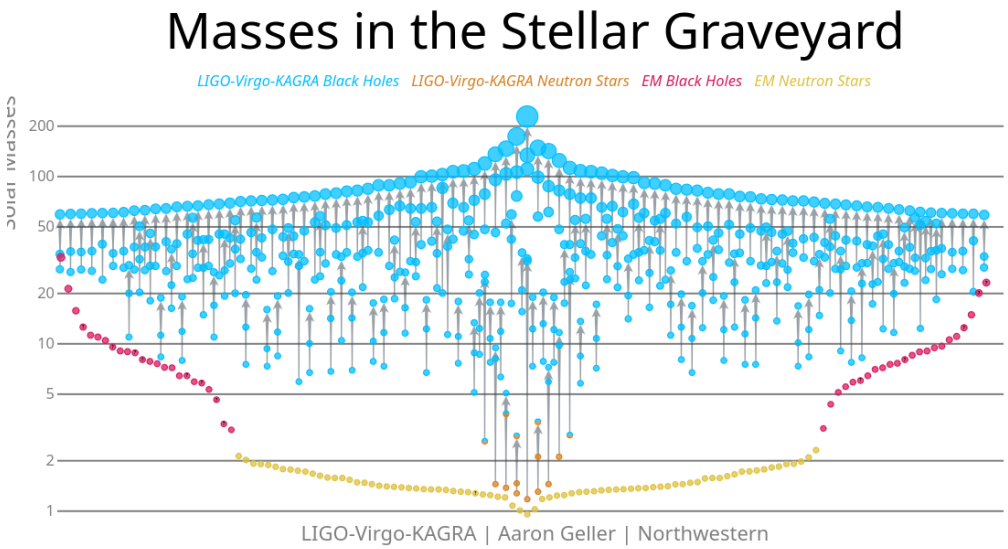

Figure 1.1: The Black Holes (BHs) and Neutron Stars (NSs) as detected through the GW and Electromagnetic (EM) channel. Credit: Aaron M. Geller, Northwestern University

[32] along with revealing BH horizon signatures [33]. In the coming years, as existing detectors become more sensitive and new observatories come online, GW signals will be observed with higher SNR in a widened frequency spectrum. Consequently, subtle physical effects will be needed to be incorporated in the waveform models in order to minimize systematic biases in parameter estimation and tests of fundamental physics.

Gravitational waves emitted during a compact binary merger carry away system's energy, angular momentum, and linear momentum. If the emission of the GWs is anisotropic, there is a non-zero flux of linear momentum which results in the recoil of the compact object formed after the merger [34–37]. During a binary BH coalescence, since most of the linear momentum is radiated near the merger [38–44] , this recoil velocity is also as termed the kick velocity. The detection of such BH kicks would provide direct evidence that the system emits linear momentum through gravitational radiation. GW190412 [45] and GW200129_065458 [46] have shown evidence for a non-zero kick velocity until now. Black hole kicks have striking astrophysical implications. When binary black holes (BBHs) merge in dense stellar clusters, their remnants can merge with other BHs in the cluster, leading to formation of heavier and heavier BHs in a process known as hierarchical mergers. Hierarchical mergers are one of the primary mechanisms proposed for forming BHs with masses above $\sim 65 M_{\odot}$. A necessary condition for the hierarchical mergers to take place is that the clusters should retain the remnant BHs and they should be close enough to merge in a Hubble time. Black hole kicks can be as large as hundreds to thousands of km s^{-1} [47–52] whereas the escape velocity of, for example, globular clusters is about $\sim 2 - 180$ km s^{-1} and that of nuclear star clusters is $\sim 10 - 1000$ km s^{-1} [53]. If the remnant BH escapes the cluster due to large kick velocity, the hierarchical

merger channel is effectively suppressed [45, 54–59].

Kicks are also crucial for the merger of supermassive black holes (SMBHs). Kicks of the order of $\sim$ 1000 km s^{-1} can exceed the escape velocity of galaxies, thus ejecting the SMBH from the host galaxy [54, 60]. Kicks, thus need to be understood well, to accurately predict the expected merger rate for LISA [60–62]. In addition, some of the gas tightly bound to a BH will remain attached even if the black hole receives a large recoil velocity. Such high-recoiling BHs could carry their gas into interstellar or intergalactic space, potentially giving rise to quasars outside the galaxies [54, 55, 63–70]. Even if the kick velocity is not high enough to eject the BH out of the galaxy, they can still displace the BH formed after the merger thus oscillating about the galaxy core for time scales as large as $\sim$ 10Myr. The amplitudes of these oscillations can be as large as $\sim$ 200 pc and thus affect the galaxy core dynamics [63, 65, 66]. Recoiling SMBHs can produce electromagnetic (EM) signatures, including shifts in broad emission lines, flaring accretion disks, tidal disruption events from nearby stars, and hyper-compact stellar systems[71]. While a few EM candidates for recoiling SMBHs have been proposed, none have been confirmed, making GW observations currently the most promising avenue for studying BH kicks [72–74].

Black hole kicks also play an important role for the waveform modeling community. They can be used as a diagnostic for checking the consistency of waveform models from different families with each other [75]. They can also be used to assess the accuracy of waveform models. Refs. [76–78] have studied the relationship between BH kicks and multipole asymmetries. In Ref. [77], the authors presented a tool for testing the performance of waveform models with multipole asymmetries which helped them fix an inconsistency in the phase definition of the phenomenological waveform model `IMRPhenomXO4a`. In Ref. [78], the authors showed neglecting subdominant asymmetries leads to differences in velocity computations upto 210 km s^{-1} and can induce introduce systematic biases in the inference of masses and spin geometry.

Traditionally, from compact binary merger GW signals, the kick has been computed using fitting formulae inspired by the Post-Newtonian (PN) theory which are calibrated to Numerical Relativity (NR) [40, 41, 43, 44, 79]. Recently, other methods have been proposed to compute the kick velocity along the line-of-sight (LoS) using Doppler Shift [80, 81] and interaction of higher harmonics [82]. A modern day approach to compute the kick velocity is using 1.) the surrogate models `NRSur7dq4Remnant` [83], `NRSur3dq8Remnant` [84] which are trained on NR simulations from the SXS catalogs, 2.) `BHPTNRSurRemnant` [85] based on BHPT simulations and 3.) `gwModel_kick_q200_GPR`, `gwModel_kick_prec_flow` [86] which are trained on NR simulations from SXS and RIT catalogs and BHPT simulations. Bustillo et al. [87] also demonstrates computing the

direction of the kick velocity using higher-harmonic modes. A complementary approach to model the complete kick profile $\mathbf{v_k}$ is to compute the linear momentum flux using a waveform approximant or the Newman Penrose scalar [75, 88, 89]. Borchers and Ohme [75] performed a systematic study to investigate the kick velocity by computing linear momentum flux using different state-of-the-art waveform models. They found that the kick velocity estimated by different waveform models was inconsistent with each other, hinting towards waveform systematics, and proposed a kick-based tuning to the models.

A perturbed BH formed after the merger of two BHs relaxes into its stable state by emitting gravitational radiation which is known as ringdown. Within the linear perturbation theory, ringdown can be modeled as a linear superposition of damped sinusoids (also known as quasi-normal modes (QNMs)). The Inspiral-Merger-Ringdown (IMR) systematics as described in Ref. [75] can be bypassed if we estimate the kick using ringdown alone. If we assume that 1.) the accumulation of kick is done before the start time of our analysis and 2.) we neglect any 'anti-kick' [42, 90], then the modification of the ringdown model to incorporate the effect of the kick becomes easier, as the kick is just a constant velocity. Results from NR simulations have shown that kicks can reach values as high as ~ 5000 km s^{-1} [47, 50, 79, 91–93]. Recently, Ref. [94] has reported that kicks can reach values as large as ~ 28000 km s^{-1} for more finely tuned spin configurations. However, since scenarios in which kicks in BBH mergers reaching above 2 percent of speed of light is rare we assume that kicks are non-relativistic. This results in modifying the ringdown waveform through 1.) Doppler shifts of the QNM frequencies [95] and 2.) aberration [96, 97] (both in the non-relativistic limit). This approach allows for less biased measurements of the remnant black hole's recoil velocity, bypassing the systematic uncertainties of full IMR models while relying solely on the late-time ringdown signal. Building on the modified ringdown model, this thesis focuses on investigating two key aspects:

- Explore the systematic biases on the model parameters when a modified waveform (hence referred to as kicked waveform) is analyzed with an unmodified waveform (hence referred to as Kerr waveform).
- To see whether we can detect the kick velocity or does it suffer from any degeneracy with other parameters.

The rest of the thesis is structured as follows. In chapter 2, we start with some theoretical background on GWs and describe the ringdown model. In chapter 3, we detail about how we will modify the ringdown model to incorporate Doppler Shift and aberration. In chapter 4, we will develop the mathematical and analytical tools that will be used for studying systematic biases and detectability prospects. In chapter 5, we will explore the systematic biases only when Doppler shift is incorporated and we will also

discuss why we can't estimate the kick using only the Doppler shift. In chapter 6, we will explore the systematic biases and detectability prospects when both Doppler shift and aberration effects are included. Finally, we will summarize, draw conclusions and discuss possible future directions in chapter 7.

Chapter 2

Gravitational Waves

2.1 Gravitational waves in Linearised gravity

In GR, Einstein's Field Equations (EFEs) are given by

$$R_{\mu\nu} - \frac{1}{2}Rg_{\mu\nu} = 8\pi T_{\mu\nu}, \tag{2.1}$$

where $R_{\mu\nu}$ is the Ricci tensor, R is the Ricci scalar, $g_{\mu\nu}$ is the metric tensor and $T_{\mu\nu}$ is the stress-energy tensor. In the linearized approximation to GR, the spacetime metric $g_{\mu\nu}$ is written as a small perturbation about flat Minkowski spacetime

$$g_{\mu\nu} = \eta_{\mu\nu} + h_{\mu\nu}, \qquad |h_{\mu\nu}| \ll 1. \tag{2.2}$$

where $\eta_{\mu\nu}$is the Minkowski metric and $h_{\mu\nu}$represents a small perturbation. Under Lorentz transformations of the background spacetime, $h_{\mu\nu}$ transforms as a rank-two tensor. Thus, it can be interpreted as a tensor field propagating on a fixed flat background. The perturbation $h_{\mu\nu}$ initially contains ten independent components. However, not all of these correspond to physical degrees of freedom; some can be eliminated through appropriate gauge choices. Imposing the *Lorenz* gauge condition, $\partial^{\nu}\bar{h}_{\mu\nu} = 0$, where $\bar{h}_{\mu\nu} = h_{\mu\nu} - (\eta_{\mu\nu}h/2)$ is the trace reversed metric perturbation with $h = \eta^{\mu\nu}h_{\mu\nu}$, EFEs reduce to the simple wave equation.

$$\Box\bar{h}_{\mu\nu} = -\frac{16\pi G}{c^4}T_{\mu\nu}, \tag{2.3}$$

where $\Box$ is the d'Alembertian operator. In vacuum, Eqn. (2.3) reduces to

$$\Box \bar{h}_{\mu\nu} = 0, \tag{2.4}$$

which admit plane-wave solutions of the form (traveling in the $\boldsymbol{k}$ direction)

$$\bar{h}_{\mu\nu} = A_{\mu\nu} e^{ik_\alpha x^\alpha}, \tag{2.5}$$

with $k^\alpha = (\omega/c, \boldsymbol{k})$ and $\omega/c = |\boldsymbol{k}|$. Two important features follow from this result; First, since the d'Alembertian operator is given by $\Box = -(1/c^2)\partial_t^2 + \nabla^2$, Eqn. 2.4 implies that GWs travel at the speed of light. Second the Lorenz gauge condition imposes $A^{\mu\nu}k_\nu = 0$ which implies that GWs are transverse i.e. the perturbation is orthogonal to the direction of propagation. The Lorenz gauge has imposed four conditions effectively reducing the number of degrees of freedom from ten to six.

While staying in the Lorenz gauge, the degrees of freedom can be further reduced by a coordinate transformation of the form $x^\mu \to x^\mu + \xi^\mu$ with

$$\Box \xi_\mu = 0. \tag{2.6}$$

This boils down to the set of conditions

$$h^{0\mu} = 0, \qquad h^i{}_i = 0, \qquad \partial^j h_{ij} = 0, \tag{2.7}$$

which is known as the *transverse-traceless* (TT) gauge. The TT gauge (Eqn. 2.6) further reduces the degrees of freedom by four which leaves us with two degrees of freedom. Denoting the metric in TT gauge by $h^{TT}_{\mu\nu}$ and rotating the frame such that $\boldsymbol{k}$ points in the $z-$ direction (i.e. $k^\alpha = (\omega/c, 0, 0, -\omega/c)$), we get

$$A^{TT}_{\mu\nu} = \begin{pmatrix} 0 & 0 & 0 & 0 \\ 0 & A_{xx} & A_{xy} & 0 \\ 0 & A_{xy} & -A_{xx} & 0 \\ 0 & 0 & 0 & 0 \end{pmatrix}. \tag{2.8}$$

Rewriting $A_{xx} = A_+$ and $A_{xy} = A_\times$, we get $h_+ = A_+ e^{ik_\alpha x^\alpha}$ and $h_\times = A_\times e^{ik_\alpha x^\alpha}$. We therefore get

$$h^{TT}_{\mu\nu} = h_+ e^+_{\mu\nu} + h_\times e^\times_{\mu\nu}, \tag{2.9}$$

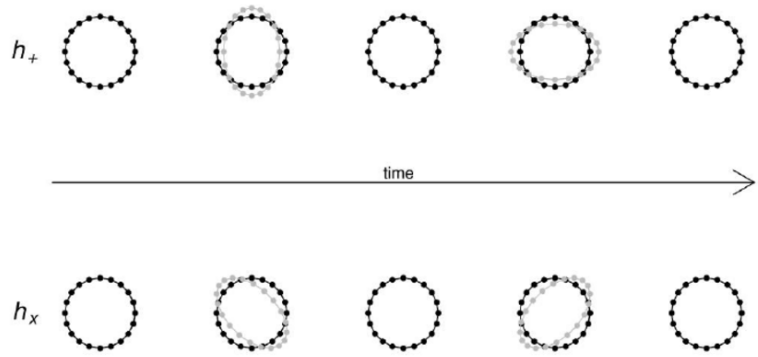

Figure 2.1: The deformation of a ring of test masses due to the + and × polarizations incident orthogonally. Image taken from Ref. [98].

where $e^+_{\mu\nu}$ and $e^\times_{\mu\nu}$ are the polarization tensors and are given by

$$e^+_{\mu\nu} = \begin{pmatrix} 0 & 0 & 0 & 0 \\ 0 & 1 & 0 & 0 \\ 0 & 0 & -1 & 0 \\ 0 & 0 & 0 & 0 \end{pmatrix}, \qquad e^\times_{\mu\nu} = \begin{pmatrix} 0 & 0 & 0 & 0 \\ 0 & 0 & 1 & 0 \\ 0 & 1 & 0 & 0 \\ 0 & 0 & 0 & 0 \end{pmatrix}. \tag{2.10}$$

For a wave traveling in a general direction n^i, we can obtain h^{TT}_{ij} by

$$h^{TT}_{ij} = \left[P^l_i P^m_j - \frac{1}{2} P_{ij} P^{lm} \right] h_{lm} \tag{2.11}$$

where $P^i_j = \delta^i_j - n^i n_j$ is the projection operator and all the indices can take the values (1,2,3).

2.2 Gravitational Wave Strain

The interaction of GW polarizations with a ring of freely falling test masses is illustrated in Fig. 2.1. As a GW propagates perpendicular to the plane of the ring, it produces time-dependent quadrupolar distortions in the proper separations between the masses. The two independent polarization states generate distinct deformation patterns and are therefore referred to as the "+" and "×" polarizations. In ground-based laser interferometric detectors such as LIGO, the suspended mirrors at the ends of the orthogonal arms serve as effective test masses. A passing GW induces a differential change in the arm lengths, which is measured with high precision through laser interferometry. The

detector output is thus directly sensitive to the strain produced by the incident GW.

Gravitational Wave detectors measure the strain $h(t)$ by measuring the fractional change in the difference between the arm lengths δL_1 and δL_2. It is written as a scalar product

$$h(t) = \frac{\delta L_1 - \delta L_2}{L} = \frac{1}{2} h_{ik}(t)(n_1^i n_1^k - n_2^i n_2^k) \equiv \overset{\leftrightarrow}{h} \cdot \overset{\leftrightarrow}{D}, \tag{2.12}$$

where $\overset{\leftrightarrow}{D} = (\boldsymbol{n_1} \otimes \boldsymbol{n_1} - \boldsymbol{n_2} \otimes \boldsymbol{n_2})/2$ is the Detector tensor and $\overset{\leftrightarrow}{h} = h_+ \overset{\leftrightarrow}{e}^+ + h_\times \overset{\leftrightarrow}{e}^\times$ is the wave tensor. The response of the detector is therefore given by

$$h(t) = h_+(t, \boldsymbol{\lambda}) F_+(\psi, \theta, \phi) + h_\times(t, \boldsymbol{\lambda}) F_\times(\psi, \theta, \phi), \tag{2.13}$$

where $F_{+,\times}$ are the antenna pattern functions. For BBH mergers in a quasi-circular orbit, the strain $h(t)$ depends on 15 parameters $\boldsymbol{\theta} = \{m_1, m_2, \chi_{1,i}, \chi_{2,i}, d_L, t_c, \varphi_c, \alpha, \delta, \iota, \psi\}$, where $m_{1,2}$ are the masses of the BHs, $\chi_{1,i}$ and $\chi_{2,i}$ are the dimensionless spins of the BHs, d_L is the luminosity distance to the source, t_c is the time of coalescence, φ_c is the coalescence phase, (α, δ) are the right ascension and declination respectively which together constitute the sky location, ι is the angle between the line of sight (LoS) and the angular momentum vector and ψ is the polarization angle.

The polarizations can be combined to form the complex amplitude $H = h_+ + i h_\times$. This complex amplitude can be decomposed into angular and temporal components. The angular dependence characterizes the radiation pattern, and hence the geometrical structure of the source, while the time-dependent coefficients describe the dynamical evolution of the system. The angular decomposition is done in terms of spin weighted spherical harmonics (SWSHs) ${}_sY^{l,m}(\iota, \varphi_0)$ of spin weight -2:

$$H(t; \lambda, \iota, \varphi_0) = \sum_{\ell=2}^{\infty} \sum_{m=-\ell}^{+\ell} H^{\ell,m}(t; \lambda)\ {}_{-2}Y^{\ell,m}(\iota, \varphi_0), \tag{2.14}$$

where $H^{\ell,m}$ are the $(\ell, m)-$modes of the GW and depend on time and intrinsic parameters and luminosity distance, together denoted by λ. (ι, φ_0) is the location of the observer as seen from the source.[1] The modes are defined as

$$H^{\ell,m} := \int H(t; \lambda, \iota, \varphi_0)\ {}_{-2}\bar{Y}^{\ell,m}(\iota, \varphi_0) d\Omega, \tag{2.15}$$

where ${}_{-2}\bar{Y}^{\ell,m}(\iota, \varphi_0)$ is the complex conjugate of ${}_{-2}Y^{\ell,m}(\iota, \varphi_0)$ and $d\Omega$ represents the elemental solid angle and the integration is over the limits $(\iota, \varphi_0) \in [0, \pi] \times [0, 2\pi)$.

[1] φ_0 can also be considered as the initial phase of the orbit.

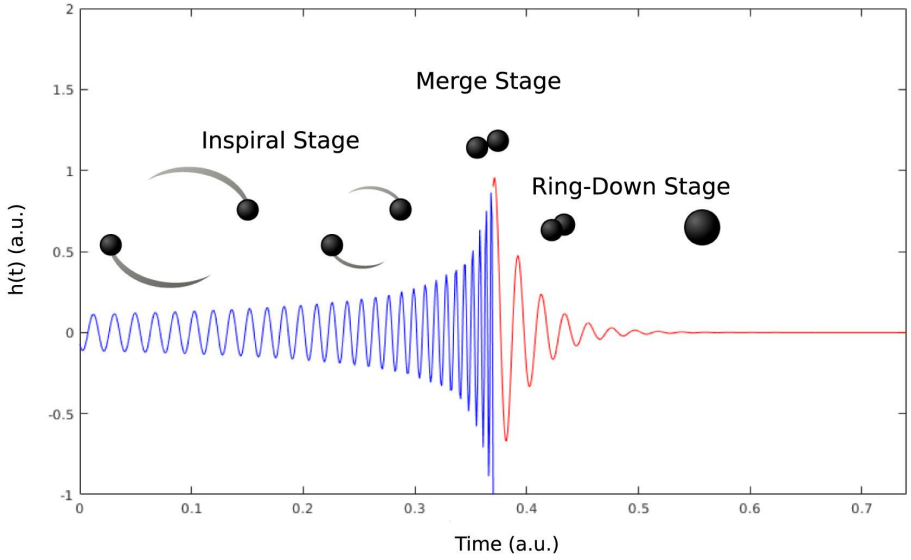

Figure 2.2: Different stages of a BBH merger: inspiral, merger and ringdown. Image taken from Ref. [99].

2.3 The Ringdown Model

The GW strain from a BBH merger, can be split into three stages: inspiral, merger and ringdown. The inspiral stage corresponds to the two BHs slowly spiraling inwards towards each other, the merger stage corresponds to the highly non-linear stage where the BHs are merging and the ringdown corresponds to the stage where the newly formed BH goes from a perturbed state to an equilibrium. Since, this thesis focuses exclusively on the ringdown phase, we now present a detailed discussion of the corresponding ringdown waveform model.

Linear Black Hole Perturbation Theory (BHPT) has been employed to study the GWs emitted from a perturbed BH. Leaver [100] proved that each multipolar component of the waveform in Eqn. 2.14 at intermediate times–after the "prompt response" and before the onset of power-law tails–is described by

$$H^{\ell,m} = \sum_{n=0}^{\infty} A_{\ell,m,n} e^{-i(\omega_{\ell,m,n}(t-t_0)+\phi_{\ell,m,n})}, \tag{2.16}$$

where t_0 is some arbitrary start time. The oscillations are called Quasi-Normal Modes (QNMs), because unlike the normal modes, these are exponentially decaying modes (for reviews on the subject, refer [101]). $\omega_{\ell,m,n} = 2\pi f_{\ell,m,n} - i/\tau_{\ell,m,n}$ is the complex frequency whose real part is the mode frequency and the inverse of the imaginary part is the damping time. In the linearised theory, the complex frequencies are completely determined by the BH properties and do not depend on the nature of the perturbation. No-hair theorem,

thus dictates that the frequencies are then completely characterised by the mass (M_f) and spin (χ_f) of the BH.

The QNMs always come "in pairs". For a Kerr BH, for a given (ℓ, m) and a given value of $a = \chi_f M_f$ the eigenvalue problem admits two solutions: one with positive real part of the frequency, the other with negative real part of the frequency and different damping time. They are the "regular" and "mirror" QNMs respectively (refer Fig. 1.6 of Ref. [102]).[2] Denoting the mirror QNM frequency with a prime, they are related to the regular frequencies by

$$\begin{aligned} f'_{\ell mn} = -f_{\ell -mn}, \quad \tau'_{\ell mn} = \tau_{\ell -mn}, \\ \implies \omega'_{\ell mn} = -\omega^*_{\ell -mn}. \end{aligned} \tag{2.17}$$

Writing $Q_{\ell mn} = \pi f_{\ell mn} \tau_{\ell mn}$ where $Q_{\ell mn}$ is the quality factor, Ref. [103] gave simple fitting functions for the quality factor and the frequency which can be inverted to obtain the mass and the spin of the BH:

$$\mathcal{F}_{\ell mn} = M_f \; f_{\ell mn} = f_1 + f_2 (1 - \chi_f)^{f_3}, \tag{2.18}$$

$$Q_{\ell mn} = q_1 + q_2 (1 - \chi_f)^{q_3}. \tag{2.19}$$

The amplitude $A_{\ell,m,n}$ and the phase $\phi_{\ell,m,n}$ are determined by the astrophysical process causing the perturbation and in the case of a BBH merger, would depend on the properties of progenitors BHs. Each (ℓ, m) mode contains an infinite number of damped sinusoids characterised by the overtone index n. The real parts of the complex frequencies of all of them are almost the same but the damped sinusoids are numbered in such a way that the $\tau_{\ell,m,n} > \tau_{\ell,m,n+1}$ for all n. Green's function techniques imply that the amplitudes $A_{\ell,m,n}$ can be factorized as a product of complex 'excitation factors' $E_{\ell,m,n}$ which depend only on the remnant mass and spin and complex-valued, initial data dependent integrals $I_{\ell,m,n}$.

Even though the angular decomposition of GWs is done in terms of SWSHs, they are not ideal for studying the perturbations of a Kerr BHs that are formed after a BBH merger. Teukolsky showed that it is most conveniently studied in terms of spin-weighted *spheroidal* harmonics ${}_sS^{\ell,m}(\iota, \varphi; a\omega)$ instead of SWSHs, so that the ringdown waveform is

$$H(t; \lambda, \iota, \varphi_0) = \sum_{\ell=2}^{\infty} \sum_{m=-\ell}^{+\ell} \sum_{n=0}^{\infty} A_{\ell,m,n} \; e^{-i(\omega_{\ell,m,n}(t-t_0)+\phi_{\ell,m,n})} \; {}_{-2}S^{\ell,m}(\iota, \varphi_0; c_{\ell,m,n}) \tag{2.20}$$

[2] They can be alternatively split into prograde and retorgrade modes which have a physical meaning: prograde (retrograde) modes are those that are corotating (counterrotating) with the spin of the BH.

Here, (ι, φ_0) is the sky location of the observer from the source and $c_{\ell,m,n} = a\omega_{\ell,m,n}$ is the oblateness parameter which depends on the BH spin $a = M_f\chi_f$ and the complex frequency $\omega_{\ell,m,n}$. In the limit $c \to 0$, the spheroidal harmonics reduce to SWSHs. To then relate the two decompositions, one can express the spheroidal harmonics in terms of spherical harmonics,

$$ {}_sS^{\ell,m}(\iota, \varphi_0; c) =_s Y^{\ell,m}(\iota, \varphi_0) + \sum_{\ell \neq \ell'} C_{\ell,\ell',m}(c) {}_sY^{\ell',m}(\iota, \varphi_0), \tag{2.21} $$

where $C_{\ell,\ell',m}(c)$ are the spherical-spheroidal mode-mixing coefficients and hence we arrive at

$$ H^{\ell,m} = \sum_{n,\ell'} A_{\ell,m,n} e^{-i(\omega_{\ell,m,n}(t-t_0)+\phi_{\ell,m,n})} C_{\ell,\ell',m}(c). \tag{2.22} $$

The waveform therefore is

$$ H(t; \lambda, \iota, \varphi_0) = \sum_{\ell=2}^{\infty} \sum_{m=-\ell}^{+\ell} \sum_{n=0}^{\infty} \sum_{\ell'=\ell_{min}}^{\infty} A_{\ell,m,n}\ e^{-i(\omega_{\ell,m,n}(t-t_0)+\phi_{\ell,m,n})} C_{\ell,\ell',m}(c)\ {}_{-2}Y^{\ell',m}(\iota, \varphi_0), \tag{2.23} $$

where $\ell_{min} = \max(|m|, |s|)$.

As we will see in section 3.1.1, aberration also induces mode-mixing between different modes. To isolate the effect on the systematic biases and detectability prospects caused by mode-mixing due to aberration, we will ignore mode-mixing due to spheroidal harmonics. That is, we will decompose the ringdown waveform in terms of spherical harmonics and not spheroidal harmonics. Although the validity of this assumption starts to break down as we increase the spin of the BH, this will be a first step in understanding the role of mode-mixing due to aberration.

Chapter 3

Black Hole kicks

Since GWs emit linear momentum, anisotropic emission will lead to the emission of a non-zero flux of linear momentum from the system. The anisotropy in the emission comes due to some inherent asymmetry in the system such as unequal masses, anti-aligned spins, etc. To conserve the linear momentum, a kick is imparted to the remnant black hole in the direction opposite to the flux of linear momentum, which is given by [88]

$$\frac{\mathrm{d}P_i}{\mathrm{d}t} = \lim_{r\to\infty} \frac{r^2}{16\pi} \oint \mathrm{d}\Omega \; l_i \; |\dot{h}|^2, \tag{3.1}$$

where $\mathrm{d}\Omega$ is the elemental solid angle and $\vec{l}$ is the unit radial vector. For quasi-circular binaries, the kick is a function of the mass ratio and the spins of the black holes at some initial epoch [104] . Kicks for precessing binaries (i.e. spins not aligned with the orbital angular momentum) can reach up to ~ 5000 km s^{-1} [47, 49–51, 93, 105] where as that for non-precessing (i.e. spins aligned with the orbital angular momentum) binaries can reach up to ~ 500 km s^{-1} [106, 107]. From an astrophysical point of view, kicks can largely influence the BBH merger rate [45]. For the waveform modeling community, kicks can be used as an important diagnostic to compare the waveform models from different families and to develop accurate models [75–77]. Thus in this chapter, we will see the effect of the kick on the observed ringdown waveform to correctly model the kick and look for any biases in the estimated parameters. Along with that, we will also explore if the correct modeling can detect the kick from the ringdown analysis.

3.1 Effect of kick on gravitational waveform

In this section, we discuss the modifications to the ringdown waveform due to the kick. We will refer to [96] for this section. When a moving source emits Electromagnetic (EM) waves, it is well known the frequencies of the waves are Doppler shifted in the direction of propagation. Along with it, they also exhibit the effect of aberration. Like EM waves, the speed for GWs is also finite and the same for all observers, so a correspondence between EM waves and GWs can be established. Doppler shift has been studied in great detail in the context of GWs [80, 82, 95, 104] (also refer the supplemental material with Ref. [104]) but it is only very recently that the effect of aberration has been studied in this context [96, 97, 108]. Both these effects can be studied by applying Lorentz transformation to the wave propagation vector. By applying Lorentz transformation to the wave propagation vector, we discuss how the waveform transforms from the source frame to the observer frame in which the source is moving at some 3-velocity $\boldsymbol{v}$. We adopt the units system where $c = G = 1$.

We start by introducing the reference frames employed in this analysis. Let the $z'-$axis be along the angular momentum (spin) of the remnant BH and $x'-$ and $y'-$axis in the plane perpendicular to $z'-$axis. In the polar-coordinate system, let θ' be the polar angle i.e. angle between the direction vector and the $z'-$axis and ϕ' be the azimuthal angle i.e. angle between the projection of direction vector in the $x' - y'$ plane and the $x'-$axis.[1] We consider an observer far away from the source such that the spacetime around the observer is flat except for the GWs. The remnant BH is moving at a velocity $\boldsymbol{v} = (v_x, v_y, v_z)$ in the observer frame. Set the frame of the observer (t, x, y, z) or (t, r, θ, ϕ) parallel to the frame of the source (t', x', y', z') or (t', r', θ', ϕ') in the limit of vanishing velocity.

In the observer and source frames respectively, the direction vectors of unit length (from the source to the observer) are given by $\boldsymbol{e_r} = (\sin\theta\cos\phi, \sin\theta\sin\phi, \cos\theta)$, $\boldsymbol{e'_r} = (\sin\theta'\cos\phi', \sin\theta'\sin\phi', \cos\theta')$. Therefore the 4-wave vectors are $\hat{k} = \omega(1, \boldsymbol{e_r})$ and $\hat{k}' = \omega'(1, \boldsymbol{e'_r})$. The Lorentz boost matrix is

$$\Lambda(\boldsymbol{v}) = \begin{bmatrix} \gamma & -\gamma v_x & -\gamma v_y & -\gamma v_z \\ -\gamma v_x & 1 + \frac{\gamma^2}{1+\gamma} v_x^2 & \frac{\gamma^2}{1+\gamma} v_x v_y & \frac{\gamma^2}{1+\gamma} v_x v_z \\ -\gamma v_y & \frac{\gamma^2}{1+\gamma} v_x v_y & 1 + \frac{\gamma^2}{1+\gamma} v_y^2 & \frac{\gamma^2}{1+\gamma} v_y v_z \\ -\gamma v_z & \frac{\gamma^2}{1+\gamma} v_x v_z & \frac{\gamma^2}{1+\gamma} v_y v_z & 1 + \frac{\gamma^2}{1+\gamma} v_x^2 \end{bmatrix}, \tag{3.2}$$

[1] In standard GW convention, θ' corresponds to ι (inclination angle).

where $\gamma = \sqrt{1-v^2}$ is the Lorentz factor. In this setup, the 4-vectors transform in the following way

$$S \underset{\Lambda(\boldsymbol{v})}{\overset{\Lambda(-\boldsymbol{v})}{\rightleftarrows}} O. \tag{3.3}$$

Applying Lorent boost $\hat{k}' = \Lambda(\boldsymbol{v})\hat{k}$, we get the time component to be

$$\begin{aligned}
\hat{k}'_0 &= \omega(\gamma + (-\gamma v_x \boldsymbol{e_{r_1}} - \gamma v_y \boldsymbol{e_{r_2}} - \gamma v_z \boldsymbol{e_{r_3}})) \\
&= \omega\gamma(1 - \langle \boldsymbol{v}, \boldsymbol{e_r} \rangle) \\
\implies \omega' &= \omega\gamma(1 - \langle \boldsymbol{v}, \boldsymbol{e_r} \rangle) \\
\implies \omega &= \frac{\omega'}{\gamma(1 - \langle \boldsymbol{v}, \boldsymbol{e_r} \rangle)} = \frac{\omega'}{\gamma(1 - v_r)},
\end{aligned} \tag{3.4}$$

where $\langle \cdot, \cdot \rangle$ is the Euclidean dot product and $v_r := \langle \boldsymbol{v}, \boldsymbol{e_r} \rangle = v_x \sin\theta\cos\phi + v_y \sin\theta \sin\phi + v_z \cos\theta$ is the velocity along the Line of Sight (LoS) and is a function of the angles (θ, ϕ). This is the standard relativistic Doppler shift for a source moving at an arbitrary direction.[2]

The first spatial component of the wave vector will be

$$\begin{aligned}
\hat{k}'_1 &= \omega \left[-\gamma v_x + \left(1 + \frac{\gamma^2}{1+\gamma} v_x^2\right) \boldsymbol{e_{r_1}} + \frac{\gamma^2}{1+\gamma} v_x v_y \boldsymbol{e_{r_2}} + \frac{\gamma^2}{1+\gamma} v_x v_z \boldsymbol{e_{r_3}}) \right] \\
&= \omega \left[-\gamma v_x + \boldsymbol{e_{r_1}} + \frac{\gamma^2}{1+\gamma} v_x \langle \boldsymbol{v}, \boldsymbol{e_r} \rangle \right] \\
&= \omega \left[-\gamma v_x + \boldsymbol{e_{r_1}} + \frac{\gamma^2}{1+\gamma} v_x v_r \right]
\end{aligned} \tag{3.5}$$

Similarly, the other spatial components of the wave vector will be

$$\hat{k}'_2 = \omega \left[-\gamma v_y + \boldsymbol{e_{r_2}} + \frac{\gamma^2}{1+\gamma} v_y v_r \right], \tag{3.6}$$

$$\hat{k}'_3 = \omega \left[-\gamma v_z + \boldsymbol{e_{r_3}} + \frac{\gamma^2}{1+\gamma} v_z v_r \right]. \tag{3.7}$$

Therefore, the Eqns. 3.5, 3.6 and 3.7 can be combined and written as

$$\omega' \boldsymbol{e'_r} = \omega \left[-\gamma \boldsymbol{v} + \boldsymbol{e_r} + \frac{\gamma^2}{1+\gamma} v_r \boldsymbol{v} \right] \tag{3.8}$$

Substituting Eqn. 3.4, we get

$$\boldsymbol{e'_r} = \frac{\boldsymbol{e_r} - \gamma \boldsymbol{v} + \frac{\gamma^2}{1+\gamma} v_r \boldsymbol{v}}{\gamma(1 - v_r)}. \tag{3.9}$$

[2] In certain references, you might see a plus sign in the denominator. Here we have a minus sign because we have defined the direction vector from the source to the observer.

To obtain $\theta = \theta(\theta^{'}, \phi^{'}), \phi = \phi(\theta^{'}, \phi^{'})$, from the $z-$component of Eqn. 3.9, we get

$$\cos\theta' = D(\theta, \phi)(\cos\theta + C(\theta, \phi)v_z). \tag{3.10}$$

where $D(\theta, \phi) := 1/\gamma(1 - v_r(\theta, \phi))$ and $C(\theta, \phi) := (\gamma^2 v_r(\theta, \phi)/(1 + \gamma)) - \gamma$. Similarly, from the $x-$ and $y-$ components, we get

$$\tan\phi' = \frac{e'_{r_y}}{e'_{r_x}} = \frac{(\sin\theta\sin\phi + C(\theta, \phi)v_y)}{(\sin\theta\cos\phi + C(\theta, \phi)v_x)}. \tag{3.11}$$

As mentioned in Ref. [96], the effect of polarization rotation does not enter at the first order, so we don't study that effect.

3.1.1 Non-relativistic limit

Since we have assumed that we will be considering non-relativistic velocities, we will be incorporating the Doppler shift and the aberration effect in the waveform only up to the first order in v. To first order in v, Eqns. 3.4 and 3.9 respectively reduce to

$$\omega = \omega'(1 + v_r), \tag{3.12}$$

$$\boldsymbol{e'_r} = \boldsymbol{e_r}(1 + v_r) - \boldsymbol{v}, \tag{3.13}$$

where according to our convention, v_r is positive if it is directed towards the observer. Let $\mathcal{A}$ be the operation for aberration by which the wave in the source frame transforms to the observer frame, so that we have $H'(\theta, \phi) = \mathcal{A}H(\theta^{'}, \phi^{'})$. Taylor expanding $H'(\theta, \phi)$ we get

$$\begin{aligned} H'(\theta, \phi) &\approx H'(\theta, \phi)\Big|_{v=0} + v\frac{\mathrm{d}H'(\theta, \phi)}{\mathrm{d}v}\Big|_{v=0} \\ &= [\mathcal{A}H(\theta^{'}, \phi^{'})]_{v=0} + v\left[\partial_{\theta'}H'(\theta, \phi)\frac{\mathrm{d}\theta'}{\mathrm{d}v}\Big|_{v=0} + \partial_{\phi'}H'(\theta, \phi)\frac{\mathrm{d}\phi'}{\mathrm{d}v}\Big|_{v=0}\right]. \end{aligned}$$

Since $\theta'|_{v=0} = \theta$ and $\phi'|_{v=0} = \phi$, we get

$$\begin{aligned} H'(\theta, \phi) &= H(\theta, \phi) + v\left[\partial_{\theta'}[\mathcal{A}H(\theta^{'}, \phi^{'})]\frac{\mathrm{d}\theta'}{\mathrm{d}v}\Big|_{v=0} + \partial_{\phi'}[\mathcal{A}H(\theta^{'}, \phi^{'})]\frac{\mathrm{d}\phi'}{\mathrm{d}v}\Big|_{v=0}\right], \\ &= H(\theta, \phi) + v\left[\partial_{\theta}H(\theta, \phi)\frac{\mathrm{d}\theta'}{\mathrm{d}v}\Big|_{v=0} + \partial_{\phi}H(\theta, \phi)\frac{\mathrm{d}\phi'}{\mathrm{d}v}\Big|_{v=0}\right]. \end{aligned} \tag{3.14}$$

Using $\cos\theta' = e'_{r_z}$ and $\tan\phi' = e'_{r_y}/e'_{r_x}$, from Eqn. 3.13, we get

$$\delta\theta' = \frac{v_z - v_r\cos\theta}{\sin\theta}, \tag{3.15}$$

$$\delta\phi' = \frac{v_x\sin\phi - v_y\cos\phi}{\sin\theta}. \tag{3.16}$$

Now we have $\delta v(\mathrm{d}\theta'/\mathrm{d}v) = \delta\theta'$ and $\delta v(\mathrm{d}\phi'/\mathrm{d}v) = \delta\phi'$. Since $\delta v = v - 0 = v$, we can replace the derivatives with the quantities computed above. So Eq. 3.14 becomes

$$H'(\theta,\phi) = H(\theta,\phi) + \frac{1}{\sin\theta}\Big[\partial_\theta H(\theta,\phi)(v_z - v_r\cos\theta) + \partial_\phi H(\theta,\phi)(v_x\sin\phi - v_y\cos\phi)\Big]. \tag{3.17}$$

Using Eqn. 2.14, decompose the complex amplitude in terms of SWSHs. The angular dependence is encoded only in the SWSHs, so using their differential properties, we get

$$\begin{aligned} H'(\theta,\phi) &= \sum_{\ell=2}^{\infty}\sum_{m=-\ell}^{\ell} H^{\ell,m}\,{}_{-2}Y^{\ell,m} + \frac{1}{\sin\theta}\Big[(v_z - v_r\cos\theta)\sum_{\ell=2}^{\infty}\sum_{m=-\ell}^{\ell} H^{\ell,m}\partial_\theta({}_{-2}Y^{\ell,m}) + \\ &\qquad (v_x\sin\phi - v_y\cos\phi)\sum_{\ell=2}^{\infty}\sum_{m=-\ell}^{\ell} H^{\ell,m}\partial_\phi({}_{-2}Y^{\ell,m})\Big] \\ &= \sum_{\ell=2}^{\infty}\sum_{m=-\ell}^{\ell}\Bigg(H^{\ell,m}\,{}_{-2}Y^{\ell,m} + \frac{1}{\sin\theta}\Bigg[(v_z - v_r\cos\theta)H^{\ell,m}\left(\frac{e^{-i\phi}J_+ - e^{i\phi}J_-}{2i}\right)({}_{-2}Y^{\ell,m}) + \\ &\qquad (v_x\sin\phi - v_y\cos\phi)H^{\ell,m}im({}_{-2}Y^{\ell,m})\Bigg]\Bigg) \end{aligned} \tag{3.18}$$

Decomposing the LHS as well, we get

$$\begin{aligned} \sum_{\ell=2}^{\infty}\sum_{m=-\ell}^{\ell} H'^{\ell,m}\,{}_{-2}Y^{\ell,m} = \sum_{\ell=2}^{\infty}\sum_{m=-\ell}^{\ell} H^{\ell,m}\Bigg({}_{-2}Y^{\ell,m} + \frac{1}{\sin\theta}\Bigg[&(v_x\sin\phi - v_y\cos\phi)im({}_{-2}Y^{\ell,m}) + \\ &(v_z - v_r\cos\theta)\left(\frac{e^{-i\phi}(i\xi_+\,{}_{-2}Y^{\ell,m+1}) - e^{i\phi}(i\xi_-\,{}_{-2}Y^{\ell,m-1})}{2i}\right)\Bigg]\Bigg), \end{aligned} \tag{3.19}$$

where $\xi_\pm = \sqrt{(\ell\mp m)(\ell+1\pm m)}$. The modes can be extracted using Eqn. 2.15. Rewriting $v_x\sin\phi - v_y\cos\phi = \Im(v_- e^{i\phi}) = (v_- e^{i\phi} - v_+ e^{-i\phi})/(2i)$ where $v_\pm = v_x \pm i v_y$, we get

$$\begin{aligned} H'^{\ell,m} = H^{\ell,m} + \sum_{\ell'=2}^{\infty}\sum_{m'=-\ell'}^{\ell'} H^{\ell',m'}\Bigg[&im'\int\frac{v_- e^{i\phi} - v_+ e^{-i\phi}}{2i\sin\theta}\,{}_{-2}Y^{\ell',m'}\,{}_{-2}\bar{Y}^{\ell,m}\mathrm{d}\Omega + \\ &\frac{\xi'_+}{2}\int\frac{(v_z - v_r\cos\theta)e^{-i\phi}}{\sin\theta}\,{}_{-2}Y^{\ell',m'+1}\,{}_{-2}\bar{Y}^{\ell,m}\mathrm{d}\Omega - \end{aligned}$$

$$\frac{\xi'_-}{2}\int \frac{(v_z - v_r\cos\theta)e^{i\phi}}{\sin\theta}\,{}_{-2}Y^{\ell',m'-1}\,{}_{-2}\bar{Y}^{\ell,m}\mathrm{d}\Omega\Bigg].$$

$$\equiv H^{\ell,m} + \sum_{\ell'=2}^{\infty}\sum_{m'=-\ell'}^{\ell'} H^{\ell',m'}\left[im' I_1 + \frac{\xi'_+}{2}I_2 - \frac{\xi'_-}{2}I_3\right]. \tag{3.20}$$

After this, we proceed numerically and compute the expressions in Mathematica. As an example, we consider that the source emits all the modes up to $\ell = 10$ and compute the (2,2) mode in the observer frame. The expression as obtained from Eqn. 3.20 is

$$\begin{aligned}
H'^{\,2,2} = {} & \frac{5}{12}v_- H^{2,1} + \frac{1}{3}(3-2v_z)H^{2,2} + \frac{13}{6\sqrt{14}}v_- H^{3,1} - \frac{4}{3}\sqrt{\frac{5}{7}}\,v_z H^{3,2} + 17\sqrt{\frac{2}{105}}v_+ H^{3,3} \\
& + \frac{1}{2}\sqrt{\frac{5}{2}}v_- H^{4,1} + 4\sqrt{\frac{2}{35}}v_+ H^{4,3} + \frac{1}{4}\sqrt{\frac{55}{7}}v_- H^{5,1} + \frac{17}{14}\sqrt{\frac{11}{30}}v_+ H^{5,3} \\
& + \frac{1}{4}\sqrt{\frac{13}{2}}v_- H^{6,1} + \frac{71}{168}\sqrt{\frac{13}{5}}v_+ H^{6,3} + \frac{5}{6\sqrt{2}}v_- H^{7,1} + \frac{125}{84\sqrt{6}}v_+ H^{7,3} \\
& + \frac{1}{2}\sqrt{\frac{17}{14}}v_- H^{8,1} + \frac{211}{84}\sqrt{\frac{17}{330}}v_+ H^{8,3} + \frac{1}{4}\sqrt{\frac{95}{22}}v_- H^{9,1} + \frac{47}{264}\sqrt{\frac{133}{15}}v_+ H^{9,3} \\
& + \frac{1}{12}\sqrt{35}v_- H^{10,1} + \frac{62}{33}\sqrt{\frac{14}{195}}v_+ H^{10,3}.
\end{aligned} \tag{3.21}$$

There a few important points to note here:

- An (ℓ, m) mode in the observer frame has contributions from the modes in the source frame of the orders $m-1, m, m+1$ but of all orders $\ell' = \max(2, |m-1|), ..., \infty$. Let's make this more clear with an example. If the source emits radiation in all the $2 \leq \ell < \infty, |m| \leq \ell$ modes, then the $(2,2)$ mode in the observer frame would be a combination of $(\ell,1), (\ell,2), (\ell,3)$ modes where $2 \leq \ell < \infty$. On the other hand, if the source were to emit only $(2,2)$ mode[3], the observer would observe all the $(\ell,1), (\ell,2), (\ell,3)$ modes where $2 \leq \ell < \infty$.

- The contribution to the (ℓ, m) mode in the observer frame comes from the $m-1$ mode due to v_-, from the $m+1$ mode due to v_+ and from the m mode due to v_z. In this case, the $(\ell', 1)$ mode comes with $v_- = v_x - iv_y$, $(\ell', 2)$ mode comes with v_z and $(\ell', 3)$ mode comes with $v_+ = v_x + iv_y$.

We also obtain a numerically computed expression for the same case computed from Eqn. 32 from Ref. [96] which we don't show here. We find a schematic agreement in both the expressions however the numerical coefficients differ from each other. While

[3]In principle, the source cannot emit only $(2,2)$ mode: there will also be a $(2,-2)$ mode but just to have an understanding, consider this.

implementing the modifications due to aberration effect, we will be implementing Eqn. 3.21 to study the biases and detectability prospects.

3.1.2 Modifying the ringdown model

In this section, we will describe the final waveform that we will be using for analyzing the systematic biases and detectability prospects when both Doppler shift and aberration effect have been taken into account. Substituting Eqn. 2.16 in Eqn. 3.20, we see that in the observer frame, the ringdown mode $H'^{\ell m}$ has the form

$$\begin{aligned} H'^{\ell m} = &\sum_{n=0}^{\infty} A_{\ell,m,n} e^{-i(\omega_{\ell,m,n} t + \phi_{\ell,m,n})} \\ &+ \sum_{\ell',m'} \sum_{n=0}^{\infty} A_{\ell',m',n} e^{-i(\omega_{\ell',m',n} t + \phi_{\ell',m',n})} \left[im' I_1 + \frac{\xi'_+}{2} I_2 - \frac{\xi'_-}{2} I_3 \right] \end{aligned} \tag{3.22}$$

Considering all the modes for the analysis is computationally prohibitive, hence we consider only the most dominant modes in the source frame which are the (220) and (330) modes. Incorporating the Doppler shift as well, Eqn. 3.21, reduces to

$$\begin{aligned} [H_{22}]_{obs} = &\left(1 - \frac{2}{3} v_z\right) \left[A_{220} e^{-i(\omega_{220}(t-t_0)(1+v_r)+\phi_{220})} \right]_{src} + \\ &\left(17\sqrt{\frac{2}{105}}\right) \left[A_{330} e^{-i(\omega_{330}(t-t_0)(1+v_r)+\phi_{330})} \right]_{src} (v_x + i v_y). \end{aligned} \tag{3.23}$$

This will be the model that we will be using in chapter 6 to investigate systematic biases and detectability prospects.

After describing the computational tools for the analysis in the next chapter, we will perform the analysis step-by-step. That is first we will only incorporate the Doppler shift in the model in chapter 5. We will then go on to incorporating both Doppler shift and aberration in chapter 6.

Chapter 4

Bayesian Parameter Estimation

After studying the modifications to the waveform, we now turn to the analysis of the signal within the realistic framework of detector noise. In GW data analysis, matched filtering is employed to search for signals buried in noisy data. More precisely, the detection procedure is based on maximizing the likelihood (or equivalently, the log-likelihood) of the data given a signal model under the assumption of stationary Gaussian noise. The matched-filter signal-to-noise ratio (SNR) naturally arises from this likelihood formalism and serves as a convenient detection statistic. Once a GW signal has been identified through search pipelines, the next objective is to determine the nature of the source and its physical configuration. This requires estimating the parameters of the system that generated the observed signal. Parameter estimation is challenging because the detector data contains both the GW signal and instrumental noise. Consequently, the source parameters are inferred within the framework of Bayesian inference. This approach provides not only the most probable values of the parameters but also their associated statistical uncertainties arising from detector noise. We discuss the basic time domain Bayesian inference technique and a few important quantities we report in the remaining sections of this thesis.

4.1 Time domain Bayesian analysis

Bayesian inference is based on Bayes' theorem, which provides a consistent rule for updating probabilities in light of new information. For two events A and B, the theorem

states

$$P(A|B) = \frac{P(B|A)P(A)}{P(B)} \tag{4.1}$$

where $P(A|B)$ is the conditional probability of A given B. In GW data analysis, we aim to infer the source parameters θ from the observed detector data d. Applying Bayes' theorem yields[1],

$$P(\theta|d) = \frac{P(d|\theta)P(\theta)}{P(d)}. \tag{4.2}$$

Here, $P(\theta|d)$ is the posterior probability density of the parameters, $P(\theta)$ is the prior distribution encoding our assumptions before analyzing the data (henceforth denoted by $\pi(\theta)$) and $P(d|\theta)$ is known as the likelihood (henceforth denoted by $\mathcal{L}(d|\theta)$) which quantifies how well a model with parameters θ explains the observed data. The denominator $P(d) = \int \mathcal{L}(d|\theta)d\theta$ is the evidence (or marginalized likelihood), denoted $\mathcal{Z}$, and ensures proper normalization of the posterior distribution.

The transient GW signals recorded in the LIGO-Virgo detectors are readily analyzed in the Fourier domain. This choice is primarily driven by the advantages it offers, particularly in the likelihood computation as the instrumental noise is well described as a stationary Gaussian process. However, frequency domain analysis has certain disadvantages when it comes to analyzing particular segments of data, especially the ringdown, as it does not meet these basic requirements: it is not possible to enforce cyclic boundary conditions which prevents the noise covariance matrix from being diagonal and it is not possible to avoid spectral leakage without corrupting the signal. In spite of these difficulties, attempts have been made to resort to full or partial Fourier domain analyses [109–112]. However, issues such as coupling of the pre-truncation point data and post-truncation point data due to overwhitening filter and spectral leakage arise which can result in the contamination of ringdown measurements. An approach to address these issues is to abandon the assumption of circular boundary conditions and work in the time domain [113]. A mathematically equivalent strategy is the *gating-and-inpainting* approach which uses a frequency domain formulation [114–116], however this approach destroys the diagonality of the Fourier covariance matrix. The efficiency of each method over the other depends on the length of the signal [101] (Refer to table 6 of Ref. [101] for a summary of different analyses techniques used). We will resort to time domain Bayesian analyses when it comes to analyzing ringdown data. We will refer to [113] for details and we will review the essential components here.

[1]Here we always assume that we know what the underlying model is i.e. given some parameters θ, we know what the signal would look like.

4.1.1 Modeling the likelihood in time domain

We first write the data d in the detector as

$$d(t) = h(t) + n(t) \tag{4.3}$$

where h is the GW signal that we expect to be there and n is the instrumental noise in the detector i.e. the data in the detector when no GW signal is present. The noise is modeled as a discrete time random process, represented by a set of random variables $n_i \equiv n(t_i)$, when sampled at times t_i. Assuming Gaussianity, the process can be completely described by its mean $E[n_k]$ (which for convenience, we can set it to zero) and its covariance matrix $C_{ij} = E[n_i n_j - E[n_k]] = E[n_i n_j]$ (with the only condition that it is positive semi-definite). For an $N-$vector $n = \{n_0, n_2 ....., n_{N-1}\}$ drawn from such a process, C will be a $N \times N$ matrix and the log-probability of the draw will be

$$\log P(n) = -\frac{1}{2} \sum_{i,j} n_i C^{-1}_{ij} n_j + \text{constant}, \tag{4.4}$$

where C^{-1} is the inverse of the covariance matrix. For a stationary random process, the covariance matrix becomes a symmetric Toeplitz matrix[2],

$$C_{ij} = \rho(|i - j|), \tag{4.5}$$

where $\rho(k)$ is the auto-covariance function (ACF), which can be estimated empirically by auto-correlating a long stretch of noise-only data.

Once we have the covariance matrix, we can analyze a noisy data $d(t)$ with a model defined after some truncation time t_{start}. Assuming the data was presampled at some set of times t_i, we will index the such that $i = 0$ corresponds to the first sample at or after the specified truncation time,

$$t_0 \equiv \min(\{t_i \ \text{ such that } t_{start} < t_i\}). \tag{4.6}$$

With this convention, the log-likelihood for data after t_{start} can be written as

$$\log P(d|n) = -\frac{1}{2} \sum_{i,j=0}^{N-1} (d_i - h_i) C^{-1}_{ij} (d_i - h_i) \tag{4.7}$$

This likelihood is completely agnostic about times before t_0. Note that it is not sufficient to set $h(t) = 0$ before t_0. Such a model predicts no signal before t_0, at which point the

[2] A Toeplitz matrix A is a matrix that satisfies $A_{i,j} = A_{i+1,j+1}$.

template turns on sharply–this is not agnostic for times before t_0. With this likelihood and appropriate prior probabilities, we can use Eqn. 4.2 to compute the posterior probability of the source parameters.

4.2 Quantities of Interest

In this section, we define some other useful quantities. We first define the SNR which is used as a detection statistic which tells us how "loud" the signal is, which will be used to compare systems with different parameters by bringing them on the same footing as far as observation is concerned. Then we define the overlap which is used to see how "similar" two waveforms are, which will be used to compare different waveforms.

4.2.1 Signal-to-Noise Ratio (SNR)

Using Eqn. 4.3, one might think that we can detect a signal only when $|h(t)| > |n(t)|$, but this is not true. If we know $h(t)$ and have an idea of the typical scales of the variations of the noise, then it can be shown that it suffices to have $h_0 > n_0\sqrt{\tau_0 T}$, where h_0 is the characteristic amplitude of $h(t)$, n_0 is the characteristic function of $n(t)$, T is the time observation and τ_0 is a typical characteristic time scale, e.g. time period of the oscillating function $h(t)$. The technique used to dig out a GW signal from a much larger noise is called matched-filtering and the quantity used in GW data analysis to measure the "loudness" of the GW signal is the Signal-to-Noise Ratio (SNR). Here we define the SNR in time domain. The uncertainties of the posterior distributions of the parameters reduce as the SNR increases.

Generically, the Signal-to-Noise Ratio (SNR) is defined as the ratio of the expectation of data when signal is present to the root-mean-square value of the data when the signal is absent. Eqn. 4.4 motivates us to define an inner product incorporating data only after t_{start}, for any two time series $x_i = x(t_i)$ and $y_i = y(t_i)$:

$$\langle x|y\rangle_{t_0} \equiv \sum_{i,j=0}^{N-1} x_i \, C_{ij}^{-1} \, y_j. \tag{4.8}$$

Using the notion of distance given by Eqn. 4.8, it can be shown that the definition of SNR boils down to the following quantity which is the optimal SNR (for an arbitrary time series x_i)

$$\mathrm{SNR}_{opt}[t_0] \equiv ||x||_{t_0} \equiv \langle x|x\rangle_{t_0}^{1/2}. \tag{4.9}$$

By the same token, the matched-filtered SNR of a signal h_i in some data $d_i = s_i + n_i$, is

$$\mathrm{SNR}_{mf}[t_0] \equiv \frac{\langle s|d\rangle_{t_0}}{\langle s|s\rangle_{t_0}^{1/2}}, \tag{4.10}$$

where t_0 in the above equations denote the truncation time and we will drop it to make the notation simpler. The matched-filtered SNR gives us a notion of the 'overlap' of the signal with the data whereas the optimal SNR gives us a notion of what the SNR we could achieve in an ideal condition (i.e. zero noise).

For multiple detectors, the SNRs are added quadratically, i.e.

$$\mathrm{SNR}_{net}[t_0] \equiv \sqrt{\sum(\mathrm{SNR}_I[t_0 + \delta t_I]^2}, \tag{4.11}$$

where the sum is over each detector I, and $\mathrm{SNR}_I[t_0 + \delta t_I]$ is the SNR at the I^{th} detector (matched filtered or optimal), evaluated at respective truncation times shifted by δt_0 with respect to t_0.

4.2.2 Overlap

In the spirit of the inner product defined in the previous section, the overlap between two time series $h(t)$ and $g(t)$ is defined as

$$\mathcal{O}(h, g) = \frac{\langle h|g\rangle}{\langle h|h\rangle \langle g|g\rangle}. \tag{4.12}$$

This quantity is used to see how 'similar' the two time series are. The mismatch between the two waveforms is then defined as

$$\mathcal{MM} = 1 - \mathcal{O} = 1 - \frac{\langle h|g\rangle}{\langle h|h\rangle \langle g|g\rangle}, \tag{4.13}$$

which tells us how 'different' are the two time series. This quantity provides us about an idea of the bias i.e. the larger the mismatch, the greater the expected bias. So this quantity will be used as an useful diagnostic before moving to parameter estimation of where in the parameter space we can expect a higher bias.

Chapter 5

Doppler Shift

Having looked at the imprints of the kick velocity on the waveform up to the first order in velocity in chapter 3, we now focus on exploring the detectability prospects of the kick and the systematic biases on the parameters if a kicked waveform is analyzed without incorporating the effects of the kick. In this chapter, we will first incorporate only the Doppler shift and then in the next chapter we will incorporate both the Doppler shift and the mode-mixing effect due to aberration. We first explore what kinds of systematic biases we have from ringdown analysis alone using the methods discussed in the previous chapter. We then discuss about the degeneracy between the final mass and the kick [95] and present a mathematical analysis of the biases observed in the Bayesian analysis. Owing to the degeneracy, we then discuss why it is not possible to detect the kick and mass simultaneously using only the ringdown analysis. We then explore the detectability prospects of the kick using a back-of-the-envelope argument where we consider that the final mass has been accurately estimated using inspiral to break the degeneracy.

5.1 Systematic biases

When analyzing real data, the most we can do is compare different waveform models and determine which provides a better fit to the observations. In the context of GW data analysis, such comparisons are typically performed using the Bayes factor (or, more generally, the odds ratio), which quantifies the relative support that the data provide for one model over another. However, with real data we cannot determine whether any inferred parameter is biased, since the true underlying model and the true parameter

values are unknown. In situations where observations of the types of systems we wish to study are not yet available or sparse, we must rely on simulated data. To assess the potential importance of a given physical effect, we therefore assume a fiducial "true" model that includes this effect and generate simulated signals based on it. We can then analyze these signals with models that either include or neglect the effect, allowing us to evaluate the impact of its omission.

In this case, we will assume that a kicked model (i.e. Doppler shifted ringdown model) will be the true model and analyze it with a Kerr model (i.e. the ringdown model which does not have the Doppler shift). The analysis will be two-fold: first we will compare the two models using overlaps to see how 'similar' the waveforms are. Here, we will be looking at the mismatches between waveforms for 3 different cases: 1.) waveform having only (2,2,0) mode, 2.) waveform having (2,2,0) and (2,2,1) modes and 3.) waveform having (2,2,0) and (3,3,0) mode. This will be a first step in understanding where in the parameter space can we expect a significant bias in the Bayesian analysis. Next, we perform Bayesian inference to quantitatively assess the bias on the parameters.

5.1.1 Mismatches: 220

We consider the ringdown model without kick is of the following form

$$h_+ + ih_\times = A_{2,2,0}\, e^{-i(\omega_{2,2,0}(t-t_0)+\phi_{2,2,0})}\ {}_{-2}Y^{2,2}(\iota,\varphi_0) \tag{5.1}$$

and the Doppler shifted model is

$$h_+ + ih_\times = A_{2,2,0}\, e^{-i(\omega_{2,2,0}(1+v_r)(t-t_0)+\phi_{2,2,0})}\ {}_{-2}Y^{2,2}(\iota,\varphi_0). \tag{5.2}$$

We look at the mismatches as a function of the final mass M_f, final spin χ_f and the kick velocity v_r (which is along the LoS) and fix all the other parameters. The fixed parameters are: $A_{2,2,0} = 1 \times 10^{-20}$, $\phi_{2,2,0} = \pi/3$, $\iota = \pi/4$ and $\varphi_0 = 0$. We compute mismatches for LIGO Hanford detector at its design sensitivity and Einstein Telescope. We use the `aLIGODesignSensitivityT1800044` and `EinsteinTelescopeP1600143` Power Spectral Densities (PSDs) from `PyCBC` to compute the ACFs using the prescription described in [113]. We compute overlaps for the waveforms as detected by detectors such that the detector is equally sensitive to both the polarizations.

In Fig. 5.1, we plot the mismatches between Kerr and kicked waveforms as a function of v_r (kick velocity along the LoS) assuming the aLIGO PSD in the top row and ET PSD in the bottom row. In the left plots we look at the mismatches as a function of

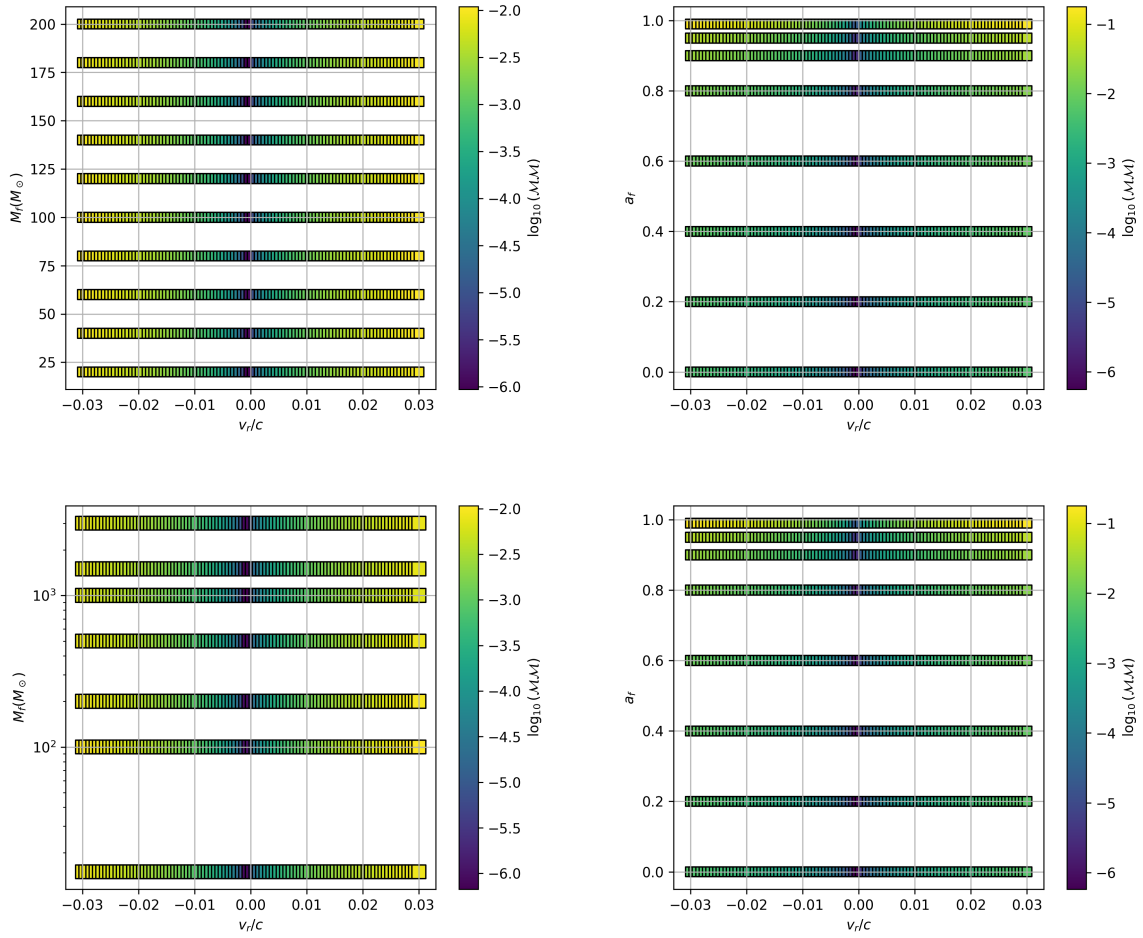

Figure 5.1: Mismatches between Kerr and kicked waveforms (only the 220 mode) assuming the aLIGO (top row) and ET (bottom row) sensitivity. Left plots show the mismatches as a function of v_r and M_f for a fixed spin $\chi_f = 0.6$. Right plots show the mismatches as a function of v_r and χ_f for a fixed mass $M_f = 100\ M_\odot$.

mass for a fixed spin value of $\chi_f = 0.6$. In the right plots we look at the mismatches as a function of spin for a fixed mass value of $M_f = 100\ M_\odot$. In all the plots we see that the mismatches increase with increase in the magnitude of kick. In the left plots, we see that, for a particular v_r, the mismatches are independent of the final mass. In the right plots, we see that, for a particular v_r, the mismatches increase with increase in spin, so the maximum mismatch is for the extremal Kerr case.

A possible explanation for this behavior is the following. Overlap is the normalised inner product of the two waveforms. So the quantity that determines the overlap is the phase difference. The phase difference between a Kerr model and a kicked model (for single mode-model) is

$$\Delta\phi_{lmn} = (2\pi f_{lmn}(t - t_0)(1 + v_r) + \phi_{lmn}) - (2\pi f_{lmn}(t - t_0) + \phi_{lmn})$$

$$= v_r 2\pi f_{lmn} t, \tag{5.3}$$

where we set $t_0 = 0$ in the last equation. Since the frequency is inversely proportional to mass and time is directly proportional to mass, the phase difference does not depend on the mass. The phase difference further is directly proportional to the the kick velocity and spin (due to the frequency). Therefore, higher is the spin or kick, more is the phase difference, lesser is the overlap and higher is the mismatch. Since frequency increases with increase in spin, mismatch increases with increase in spin. This explains the independence of mismatch with mass and the dependence on kick and spin.

5.1.2 Mismatches: 220+221

Along with the (220) mode, we consider the first overtone of the (22) mode in the model. As described in section 2.3, the overtones in a particular mode have almost the same frequency and are characterised by their damping time: $\tau_{\ell,m,n} > \tau_{\ell,m,n+1}$ for all n. So the overtone (221 mode) is a shorter lived sinusoid than the fundamental (220) mode.

$$\begin{aligned} h_+ + i h_\times = \Big[& A_{2,2,0}\, e^{-i(\omega_{2,2,0}(t-t_0)+\phi_{2,2,0})} \\ & + A_{2,2,1}\, e^{-i(\omega_{2,2,1}(t-t_0)+\phi_{2,2,1})} \Big]\ {}_{-2}Y^{2,2}(\iota, \varphi_0) \end{aligned} \tag{5.4}$$

and the Doppler shifted model will be

$$\begin{aligned} h_+ + i h_\times = \Big[& A_{2,2,0}\, e^{-i(\omega_{2,2,0}(1+v_r)(t-t_0)+\phi_{2,2,0})} \\ & + A_{2,2,1}\, e^{-i(\omega_{2,2,1}(1+v_r)(t-t_0)+\phi_{2,2,1})} \Big]\ {}_{-2}Y^{2,2}(\iota, \varphi_0). \end{aligned} \tag{5.5}$$

As done in section 5.1.1, we look at the mismatch plots as a function of the final mass M_f, final spin χ_f and the kick velocity v_r (which is along the LoS) and fix all the other parameters (values are the same as were considered in the previous subsection). In this case, now there two extra fixed parameters: the amplitude $A_{2,2,1}$ and phase $\phi_{2,2,1}$ of the (2,2,1) mode. However, they cannot be fixed arbitrarily. We will briefly review their connection with the amplitude and phase of the (2,2,0) mode and direct the reader to Ref. [117] for more details (also refer to [118–120] for more details on the subject).

As mentioned in section 2.3, the QNM's complex amplitude (i.e. $A_{\ell mn} e^{-i\phi_{\ell mn}}$) can be written as

$$C_{lmn} = I_{lmn} E_{lmn}, \tag{5.6}$$

where I_{lmn} is known as the source factor that depends on the initial-data integrals and E_{lmn} is known as the excitation factor that depends on the final mass and final spin [100, 118–123]. Now if we assume that the source term I_{lmn} is the same for all overtones i.e. does not depend on the index n ($I_{lmn} = I_{lm}$), it means that all the overtones are excited simultaneously at some time. If we let that time (relative to the peak of the strain) be t_{pert}, then we have

$$E_{(2,2,n,+)} \sim \frac{1}{I_{(2,2)}} e^{-i\omega_{(2,2,n,+)} t^{(2,2)}_{pert}} C_{(2,2,n,+)}. \tag{5.7}$$

So, we see that

$$\frac{C_{22n_1}}{C_{22n_2}} = \frac{E_{22n_1}}{E_{22n_2}} e^{i(\omega_{22n_2} - \omega_{22n_1}) t^{22}_{pert}} \tag{5.8}$$

i.e. the amplitude ratios depend only the excitation factors and the time of perturbation (when the overtones were excited). Therefore, essentially, the amplitude ratio only depends on the final spin.[1] Looking at the figures 7 (which gives magnitude of E_{22n}) and 8 (which gives the phase of E_{22n}) in Ref. [117], we approximately extract the values of the excitation factors and phases for our desired configurations. Therefore we fit just the complex amplitude for the 220 mode and complex amplitude for 221 mode can be obtained from the relation mentioned above.

We consider the same setup as described in the previous section. The values of the amplitude and phase of the (221) overtone for each case are then determined using the prescription described in the previous paragraph. In Fig. 5.2, we plot the mismatches between Kerr and kicked waveforms as a function of v_r (kick velocity along the LoS) assuming the aLIGO PSD in the top row and ET PSD in the bottom row. In the left plots we look at the mismatches as a function of mass for a fixed spin value of $\chi_f = 0.6$. In the right plots we look at the mismatches as a function of spin for a fixed mass value of $M_f = 100\ M_\odot$.

Here, we see the same trends as we see in Fig. 5.1. But, in Fig. 5.2, we see that the mismatches are lesser than the corresponding plots in the Fig. 5.1. A possible explanation for the mismatches being less is the following. Firstly, the 221 mode is a very short lived mode (it roughly dies out in a couple of cycles). Secondly, the initial amplitude of 221 mode is higher than the 220 mode, so it is the dominant mode in the early times. Now overlap is the inner product of the normalized waveforms and the overlap depends on the dephasing between the waveforms. From Eqn. 5.3 (even though it was for a single mode, it holds generally that the phase difference grows with time), we see that the phase difference increases with time. Therefore, since the 221 mode is short-lived, it dies

[1] Since it is a dimensionless quantity and it depends on the final spin and final mass only, it should not depend on the final mass.

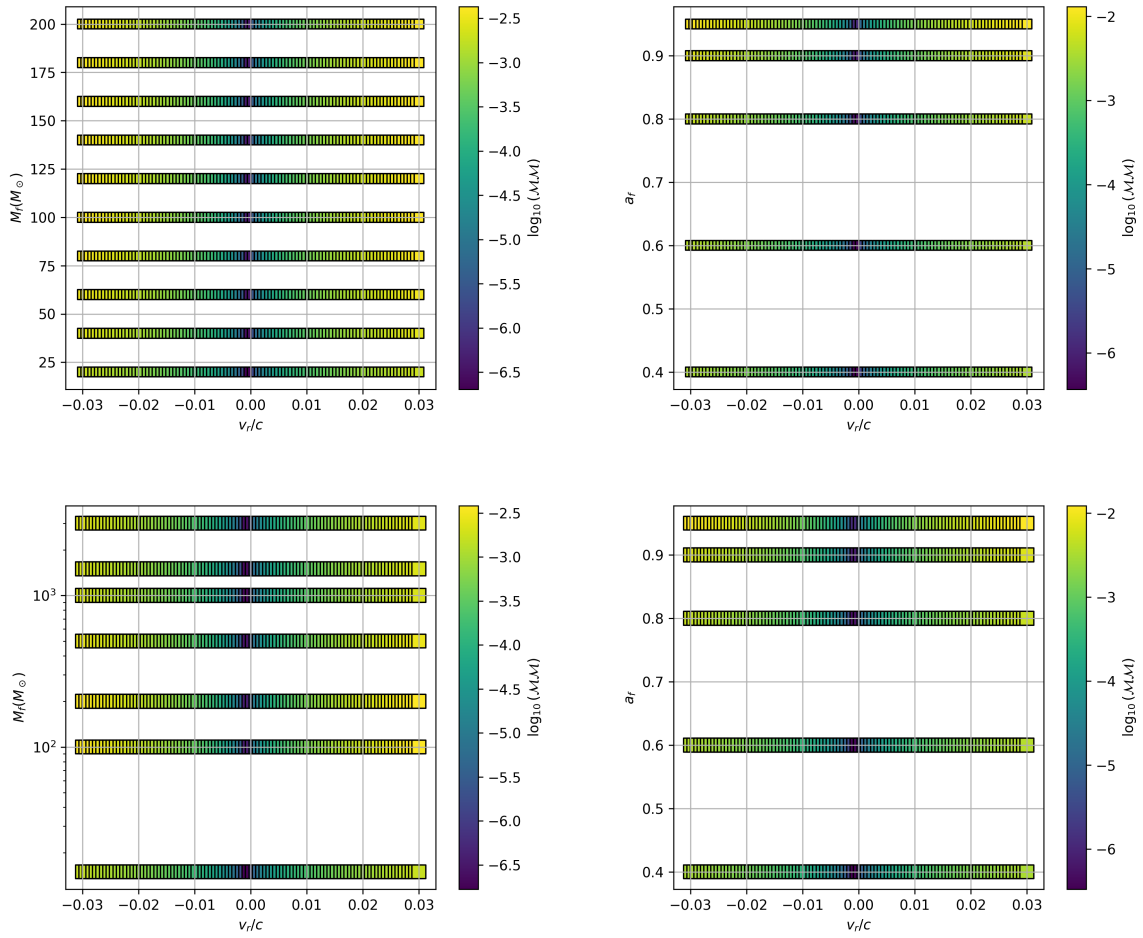

Figure 5.2: Same as Fig. 5.1 but for the overtone ringdown model.

down "before" even a significant phase difference appears. Since the (221) mode is the dominant mode in the early times, the contribution of the earlier part of the waveform to the overlap where a significant phase difference has not yet appeared increases. For the (220,221)-model, the initial part of the waveform (till some time t_1 up to which the (221) mode dies out) contributes about $\sim 99\%$ to the overlap where as in the case of the (220) only model, the contribution from the waveform till that time t_1 is about $\sim 96.5\%$. This explains the decrease in the overlaps when the (221) mode is present.

5.1.3 Mismatches: 220+330

We further want to include subdominant modes to explore the missmatch. Thus we consider the ringdown model without kick (not Doppler shifted) in this case will be

$$h_+ + ih_\times = A_{2,2,0}\, e^{-i(\omega_{2,2,0}(t-t_0)+\phi_{2,2,0})}\ {}_{-2}Y^{2,2}(\iota,\varphi_0) +$$

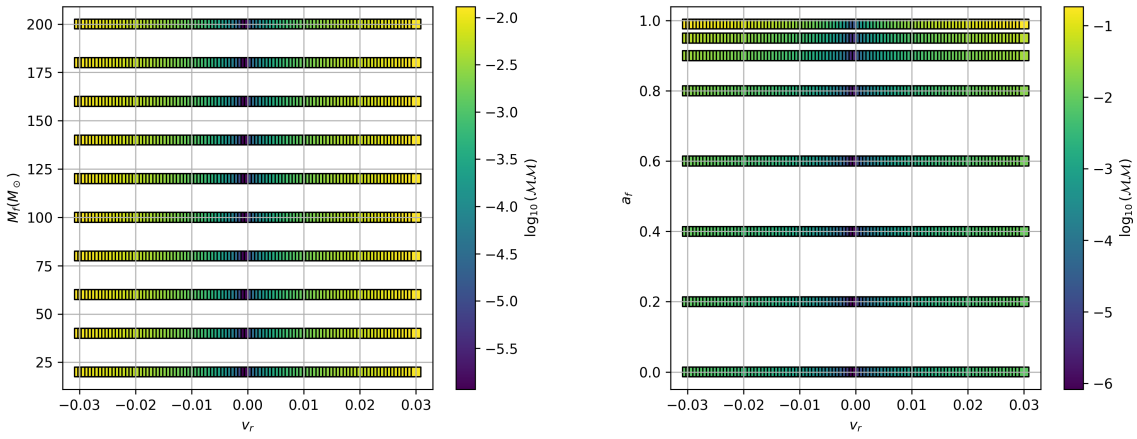

Figure 5.3: Mismatches between Kerr and kicked waveforms (having (220) and (330) modes) assuming the aLIGO sensitivity. Left plot shows the mismatches as a function of v_r and M_f for a fixed spin $\chi_f = 0.6$. Right plot shows the mismatches as a function of v_r and χ_f for a fixed mass $M_f = 100\ M_\odot$. The amplitude ratio A_{330}/A_{220} is 0.3 and the relative phase difference $\phi_{330} - \phi_{220}$ is zero in this case.

$$A_{3,3,0}\ e^{-i(\omega_{3,3,0}(t-t_0)+\phi_{3,3,0})}\ {}_{-2}Y^{3,3}(\iota,\varphi_0) \tag{5.9}$$

and the corresponding Doppler shifted model will be

$$\begin{aligned} h_+ + ih_\times = A_{2,2,0}\ e^{-i(\omega_{2,2,0}(1+v_r)(t-t_0)+\phi_{2,2,0})}\ {}_{-2}Y^{2,2}(\iota,\varphi_0) + \\ A_{3,3,0}\ e^{-i(\omega_{3,3,0}(1+v_r)(t-t_0)+\phi_{3,3,0})}\ {}_{-2}Y^{3,3}(\iota,\varphi_0). \end{aligned} \tag{5.10}$$

Unlike the case of a (220, 221)-modes model, in this case, there are fitting formulae proposed for the initial 330-mode amplitude as a function of progenitor spins and mass ratio but, to the best of our knowledge, there does not exist a "clean" model like the previous case that models the amplitude ratio of 330-mode as a function of the final spin.

As an illustrative case, we look at the mismatches for this model assuming only the aLIGO PSD and only a particular amplitude ratio. We consider the same setup as described in section 5.1.1. The (330) mode being the subdominant mode, we fix the amplitude ratio A_{330}/A_{220} to 0.3 and the initial phase difference of the modes $\phi_{330} - \phi_{220}$ to zero. In Fig. 5.3, we have plotted the mismatches for the (220, 330)-modes model. We again see the same trend as we saw in the previous cases–for a particular kick value, the mismatches are independent of the final mass and increase with increase in spin. Along with that, we see that the mismatches are greater than the 220-only case. This happens since the damping time of the (330) mode is very similar to the (220) mode and the frequency of the (330) mode is more than the (220) mode over the spin range. Since the mismatches depend on the dephasing of the waveform, higher frequency leads to higher

dephasing within a given time. Hence, we see higher mismatches for the (220,330)-modes model than the (220)-only mode model.

5.1.4 Bayesian Analysis for computing systematic bias

The mismatch analysis done in the previous subsections gives us an idea about where in the parameter space we can expect a higher bias. It reveals that the biases should not depend on the value of the final mass and they should increase with increase in the final spin. Also, the degeneracy between the kick and the final mass indicates that only the final mass will exhibit a bias. So in this section, we analyse the biases using Bayesian parameter estimation for a ringdown model with just the 220 mode. We describe the setup for Bayesian analysis. We inject Doppler shifted waveforms with nonzero kick velocities in gaussian noise in a network of LIGO Hanford and Livingston detectors at their design sensitivity. We fix the initial phase φ_0 to 0, angle of inclination ι to $\pi/4$, angle of polarisation ψ to 0, sky location (α, δ) to (2.25, 1.25) rad. To demonstrate the independence of bias on the value of the final mass, we consider two mass cases: $50M_\odot$ and $100M_\odot$ and to demonstrate the dependence of bias on the final spin, we consider five spin cases: [0.4, 0.6, 0.8, 0.9, 0.95]. We consider 13 cases of kick velocity uniformly spaced between [-0.03c, 0.03c]. We find the amplitude A_{220} and phase ϕ_{220} of the mode to fix the network SNR to 30, 50 and 100 using `scipy.optimize.minimize` function. For all these cases, during parameter estimation, we assume the kick to be zero and estimate the final mass, final spin, amplitude and phase $(M_f, a_f, A_{220}, \phi_{220})$.[2] We consider uniform priors over the final mass in the range $20 < M_f < 200$, final spin in the range $0.01 < a_f < 0.99$ and phase in the range $0 < \phi_{220} < 2\pi$. We consider a log-uniform prior over the amplitude in the range $-24 < \log(A_{220}) < -18$.

In Fig. 5.4, we plot the ratio of the systematic error to the statistical error of the final mass and final spin. The ratio is defined as

$$B_p = \frac{p_{sys}}{p_{stat}} = \frac{|p_{inj} - p_{med}|}{\sigma} \tag{5.11}$$

where σ is the standard deviation of the parameter distribution, p_{med} is the median value of the distribution and p_{inj} is the injected value. If the ratio is greater than 1, then it implies that the systematic error is more than the statistical error and hence the analysis is flawed and we will have an incorrect inference of the parameter. The left column shows the ratios for final mass and right column shows the ratios for the final spin. The top

[2]For performing the PE, we use a pipeline developed by our collaborator Dr. Akash Kumar Mishra that uses the dynesty sampler to sample the posterior distributions. Ref. [124] describes the sampling framework used in this pipeline.

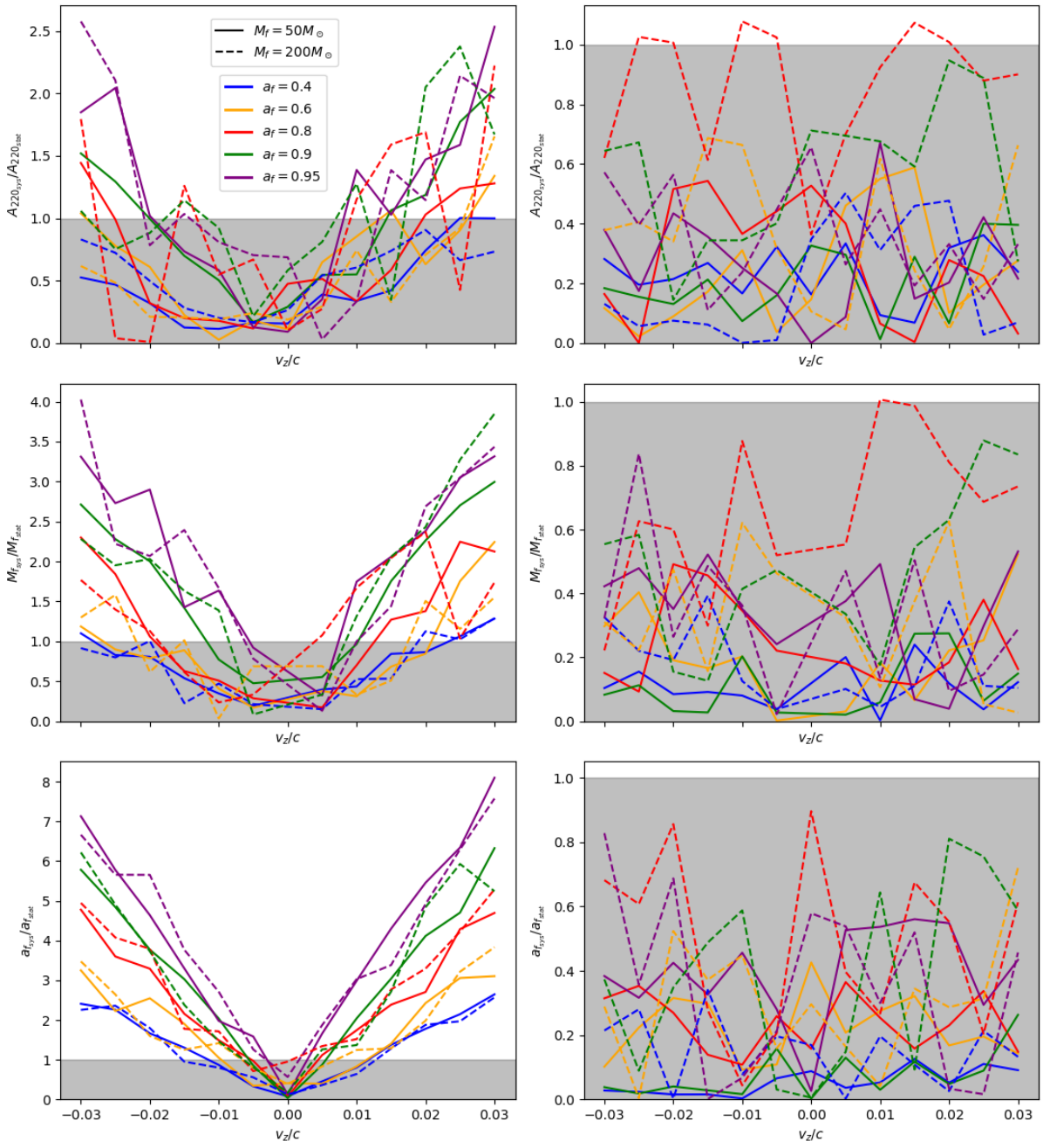

Figure 5.4: The ratios of systematic errors to the statistical errors. Left column shows the ratios for the final mass and the right column shows the ratios for the final spin. The top row shows the ratios for a network SNR of 30, middle for 50 and the bottom for 100. Line styles indicate the final mass of the system and the line colors indicate the final spin of the system in the legends of each plot. The shaded region indicates where the statistical error (1-σ error) is greater than the systematic error.

row shows the plots for a network SNR of 30, middle for 50 and the bottom one for 100.

We see that it only the final mass that is biased and not the final spin. We explain this observation in the next section. Even though not clear from the lesser SNR plots, as it was seen in the mismatch plots, the bias is independent of the value of the final mass. For a fixed kick velocity, the bias increases as the spin increases. As the SNR increases, this pattern becomes clearer and the number of systems having the systematic error greater than the statistical error increases. This happens because of the decrease in the statistical error when the SNR increases. In the network of aLIGO detectors, a kick of $\sim 0.02c$ along the line-of-sight induces significant biases on the mass for systems with $a_f > 0.8$ for a network SNR of 30, with $a_f > 0.6$ for a network SNR of 50 and with $a_f > 0.4$ for a network SNR of 100. The importance of taking the biases into account increases for 3G detectors where they are routinely expected to see ringdown signals with SNR greater than 100.

5.2 Degeneracy between kick and final mass

We see how the mass-kick degeneracy comes about in the case of ringdown model. The Doppler shift factor is $\xi = 1+v_r$ in the non-relativistic case. Therefore the Doppler-shifted frequency is $\omega^D_{\ell mn} = \xi\omega_{\ell mn}$. As we have seen before in section 2.3, $f_{\ell mn} = \alpha_{\ell mn}(\chi_f)/M_f$ and $\tau_{\ell mn} = \beta_{\ell mn}(\chi_f)M_f$ where $\alpha_{\ell mn}(\chi_f)$ and $\beta_{\ell mn}(\chi_f)$ are functions of the final spin only [103]. Therefore the Doppler-shifted frequency and damping time would be $f^D_{\ell mn} = \xi\alpha_{\ell mn}(\chi_f)/M_f$ and $\tau^D_{\ell mn} = \beta_{\ell mn}(\chi_f)M_f/\xi$. Now if we define M_f/ξ as some new quantity $M_f^{'}$, then we see that $f_{\ell mn} = \alpha_{\ell mn}(\chi_f)/M_f^{'}$ and $\tau_{\ell mn} = \beta_{\ell mn}(\chi_f)M_f^{'}$. That is this new quantity $M_f^{'}$ mimics as the final mass. Physically it means that if we don't consider the Doppler shift in our model, we will measure the mass of the system to be $M_f^{'}$ instead of M_f. We further see that the Doppler shifted ringdown model with mass M_f is exactly identical to the ringdown model without incorporating the Doppler shift with mass $M_f^{'}$. So we don't expect any other parameter than the final mass to be biased during a Bayesian analysis. This explains the observations of the biases noted in the previous section.

The second consequence of this mass-kick degeneracy is that without an independent measurement of the final mass or the kick velocity, it is not possible for us to break this degeneracy. This happens because of the absence of a length scale or a mass scale in vacuum GR. This can be better understood through the following analogy. Suppose we want to measure the frequencies of sound emitted by a moving source. What we actually measure are the Doppler shifted frequencies. We cannot infer the source frequencies and the speed of the source both from this measurement alone. We need an independent

measurement of at least one of them to infer the other solely based on the measurement of the observed frequencies. This means that if the Doppler shift is incorporated in the waveform, then because of the degeneracy, we would not be able to infer the kick velocity and the mass together.

5.3 Detectability prospects

We now explore the detectability prospects using the back-of-the-envelope argument mentioned in [80] where we assume that the final mass has been accurately estimated from the inspiral. Let M_i be the final mass as estimated from the inspiral and let M_r be the final mass as measured from the ringdown. Since we have assumed that the kick is imparted instantaneously at the merger, we can write

$$M_r = M_i(1 - v_r) \tag{5.12}$$

If we assume that the mass estimated from the inspiral is accurate i.e. we know the true mass, we can neglect the error in M_i. Differentiating the equation,we get

$$|\Delta v_r| = \frac{|\Delta M_r|}{M_i}. \tag{5.13}$$

So kicks of magnitude v_r can be detected if the final mass is measured with a fractional accuracy of $\leq v_r$. As done in the previous section, we inject signals into Gaussian noise in a network of LIGO Hanford and LIGO Livingston detectors at their design sensitivity. We fix the initial phase φ_0 to 0, angle of inclination ι to $\pi/4$, angle of polarisation ψ to 0, sky location (α, δ) to (2.25, 1.25) rad. We inject systems with different masses and different spins and find the amplitude $A_{2,2,0}$ and phase $\phi_{2,2,0}$ of the (220) mode by fixing the SNR using the same function as mentioned in previous section.

In Fig. 5.5, we look at the fractional error in mass as a function of SNR for 2 cases of the final mass: $M_f = [50M_\odot, 200M_\odot]$ which is indicated by the line style and 4 cases of final spin: $a_f = [0.4, 0.6, 0.8, 0.9]$ which is indicated by the line color. From the plots seen in the previous sections, we see that the biases are independent of the mass and it increases as we increase the spin. This is also evident from Fig. 5.5. The fractional error is independent of the final mass which implies that the detection of the kick is not affected by the mass as long as the signal lies within the detector sensitivity band. We also see that for a particular value of the SNR, the fractional error decreases as the final spin increases which implies that higher spinning systems will be more favourable for a possible detection of the kick. We would also like to note that given the initial mass ratio

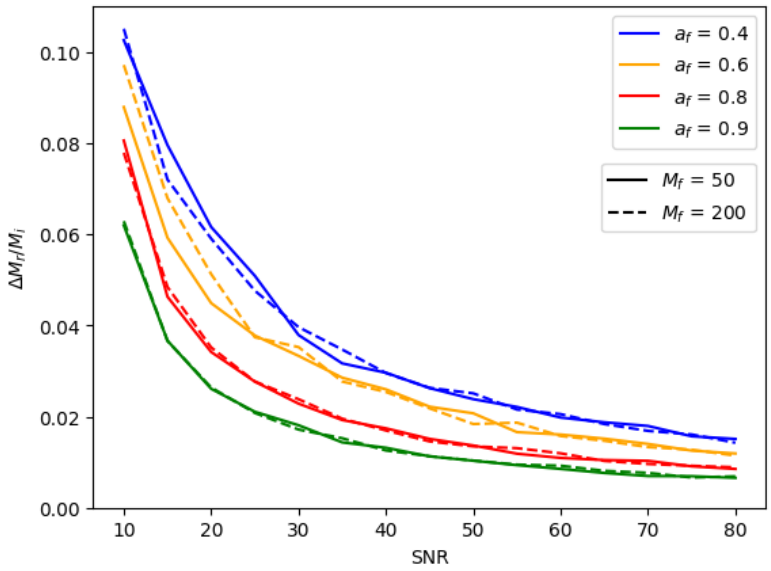

Figure 5.5: Fractional error in mass as a function of the SNR. This is shown different true final mass indicated by the line style and true final spin indicated by the line color.

and progenitor spins, fitting formulae [83, 104] also predict the final kick vector. So this method can also be used as a diagnostic to check the consistency between kick estimated from the fitting formulae and kick estimated from this method.

In this chapter, we looked at the systematic biases due to the Doppler shift and saw why it is not possible to detect the kick from the ringdown alone due to the degeneracy. In the mismatch plots, we saw that addition of an over-dominant short-lived mode on top of the (220) mode decreases the mismatch and hence configurations which excite these types of modes/overtones may not be suitable for kick detection. We also saw that addition of a sub-dominant long-lived mode increases the mismatch and hence such configurations would be favorable for kick detection. What we conclude is that the mismatch essentially depends on the lifetime of the most dominant mode in the waveform: if it is short lived, then the mismatch is low and vice-a-versa. Further, we also looked at the systematic biases on the intrinsic parameters as obtained from the Bayesian analysis for the (220)-mode only case and saw that the biases are independent of mass and increases with increase in spin. Using a back-of-the-envelope argument, we further looked at the detectability prospects of the kick if the mass is inferred from the inspiral. Having looked at the systematic biases due to the Doppler shift, we now incorporate the aberration effect in the model along with the Doppler shift.

Chapter 6

Aberration

After studying the systematic biases induced due to the Doppler shift, we now incorporate the aberration effect which induces mode-mixing and corrections to the mode amplitudes. As mentioned in section 3.1.2, we consider only the dominant and the leading subdominant mode in the source frame which are the (220) and (330) modes. Let $v_r = \vec{v} \cdot \vec{e}_r$ be the velocity along the line of sight. So the (22) mode in the observer frame will be

$$[H_{22}]_{obs} = \left(1 - \frac{2}{3}v_z\right)\left[A_{220}e^{-i(\omega_{220}(t-t_0)(1+v_r)+\phi_{220})}\right]_{src} + \left(17\sqrt{\frac{2}{105}}\right)\left[A_{330}e^{-i(\omega_{330}(t-t_0)(1+v_r)+\phi_{330})}\right]_{src}(v_x + iv_y), \tag{6.1}$$

where the subscripts *obs* and *src* mean observer and source respectively. Here, we will investigate the systematic biases for two special cases of the kick velcity: 1.)$v_x = v_y = 0, v_z \neq 0$ and 2.)$v_x = v_y = v_z$. Further, we employ Bayesian inference to investigate the detectability of the kicks and evaluate whether they can be inferred after incorporating the aberration effect.

6.1 Systematic Biases

Here, we consider two different cases to look at the systematic biases. Firstly, we consider that $v_x = v_y = 0$ and vary v_z from $-0.03c$ to $0.03c$. The model in this case will be

$$[H_{22}]_{obs} = \left(1 - \frac{2}{3}v_z\right)\left[A_{220}e^{-i(\omega_{220}(t-t_0)(1+v_r)+\phi_{220})}\right]_{src}. \tag{6.2}$$

As done in chapter 5, we inject signals in Gaussian noise considering a network of LIGO Hanford and Livingston detectors at their design sensitivity and recover them with the same ringdown model assuming kick velocity to be zero. We describe the setup of this Bayesian analysis. We fix the initial phase φ_0 to 0, angle of inclination ι to $\pi/4$, angle of polarisation ψ to 0, sky location (α, δ) to (2.25, 1.25) rad. We inject systems with different masses and different spins and find the amplitude A_{220} and phase ϕ_{220} of the (220) mode for each case by fixing the SNR using the same function as mentioned in previous chapter.

In Fig. 6.1, we plot the ratio as defined in Eqn. 5.11 on the amplitude of the 220 mode in the top row, final mass in the middle row and final spin in the bottom row for different true values of v_z. We do this for two cases of network SNR-50 and 150. From the bottom plots, we see that for the final spin, the systematic errors are always less than the statistical errors. We expect this to happen since, for this particular case, the modification due to the aberration effect comes only in the mode amplitude–the quality factor as defined in Eqn. 2.19 that determines the final spin is not affected. Further, due to Doppler shift, the systematic errors for the final mass increase with increasing kick. We see the same trends as seen in Fig. 5.4. From the top row, we also note that the mode amplitudes are biased. This is evident from the model as the modification comes in the mode amplitude. However, contrary to the plots of the final mass, we see that the biases on the amplitudes increase as the final spin decreases. We also see that the biases increase with increase in the mass. We do not have a clear explanation for these trends.

In the second case, we consider $v_x = v_y = v_z \equiv v_i$ and vary v_i from $-0.01c$ to $0.01c$. The model in this case will is given by Eqn. 6.1. We keep the same setup as the previous case. Here we have two extra parameters: the amplitude and the phase of the 330 mode. We fix the amplitude ratio of the 330 mode to the 220 mode (A_{330}/A_{220}) to 0.3 and the phase of the 330 mode to zero. As done before, we use the same ringdown model assuming kick velocity to be zero (i.e. a non-aberrated non-Doppler shifted model with just the (220) mode) to recover the injected signal.

In Fig. 6.2, we plot the ratio as defined in Eqn. 5.11 on the amplitude of the 220 mode in the top row, final mass in the middle row and final spin in the bottom row for different true values of $v = v_i\sqrt{3}$. We do this for two cases of SNR-50 and 150. For the biases in final mass in the middle row, we see the same trends as seen in Fig. 6.1 and 5.4. In the bottom row, we see that the systematic error for the final spin can be more than the statistical error. This happens since we are trying to recover a two-mode model with a one-mode model. Beyond the Doppler shift, the frequency profile of the waveform changes due to the addition of two modes and hence the spin recovery is affected. As for the ratios of the errors of the amplitudes, we see that they are comparable in value

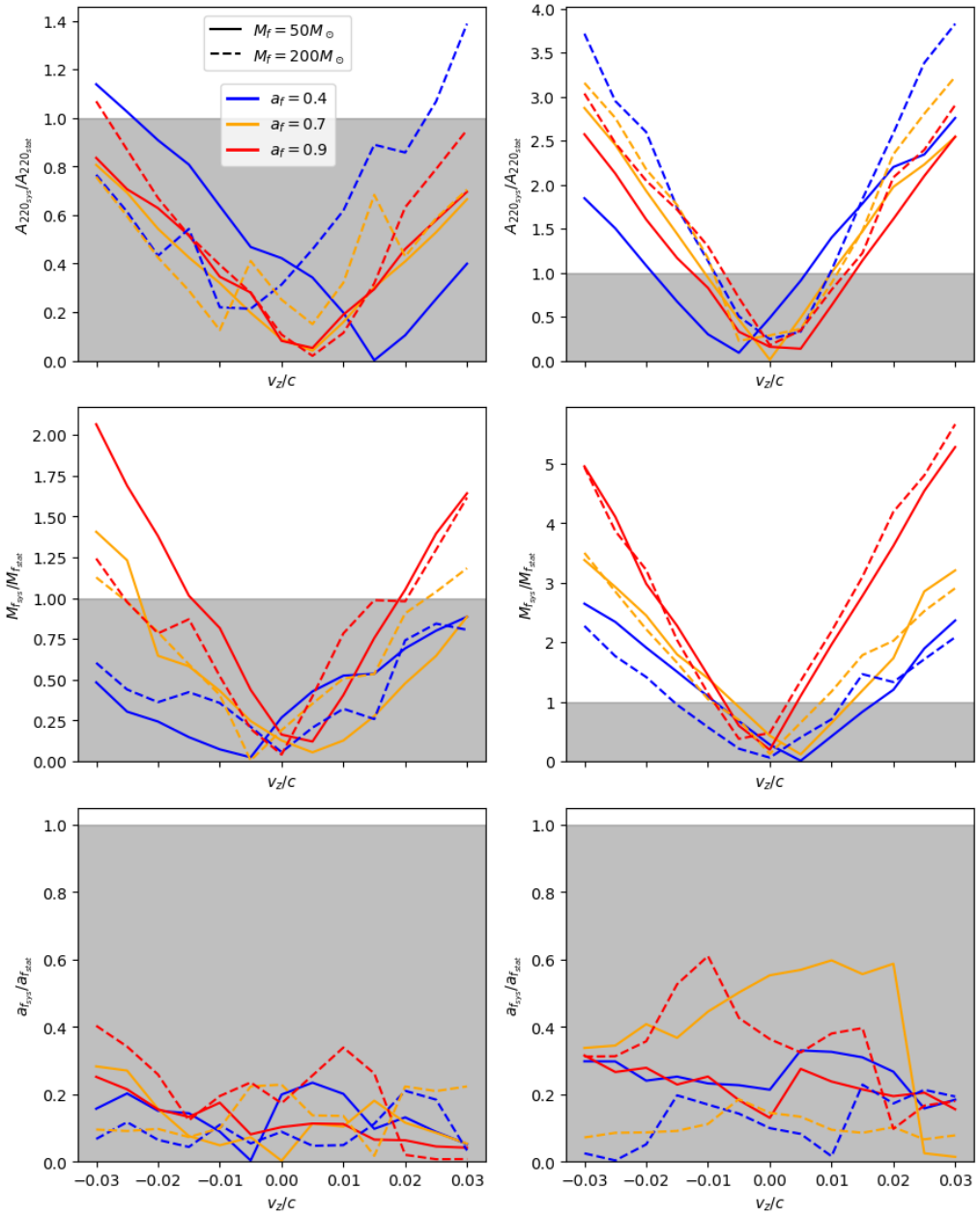

Figure 6.1: The ratios of systematic errors to the statistical errors of the amplitude, final mass and final spin for the model in Eqn. 6.2 in the top, middle and bottom rows respectively. Left (right) column shows the ratios for a network SNR of 50 (150). Line styles indicate the final mass of the system and the line colors indicate the final spin of the system in the legends of each plot. The shaded region indicates where the statistical error (1-σ error) is greater than the systematic error.

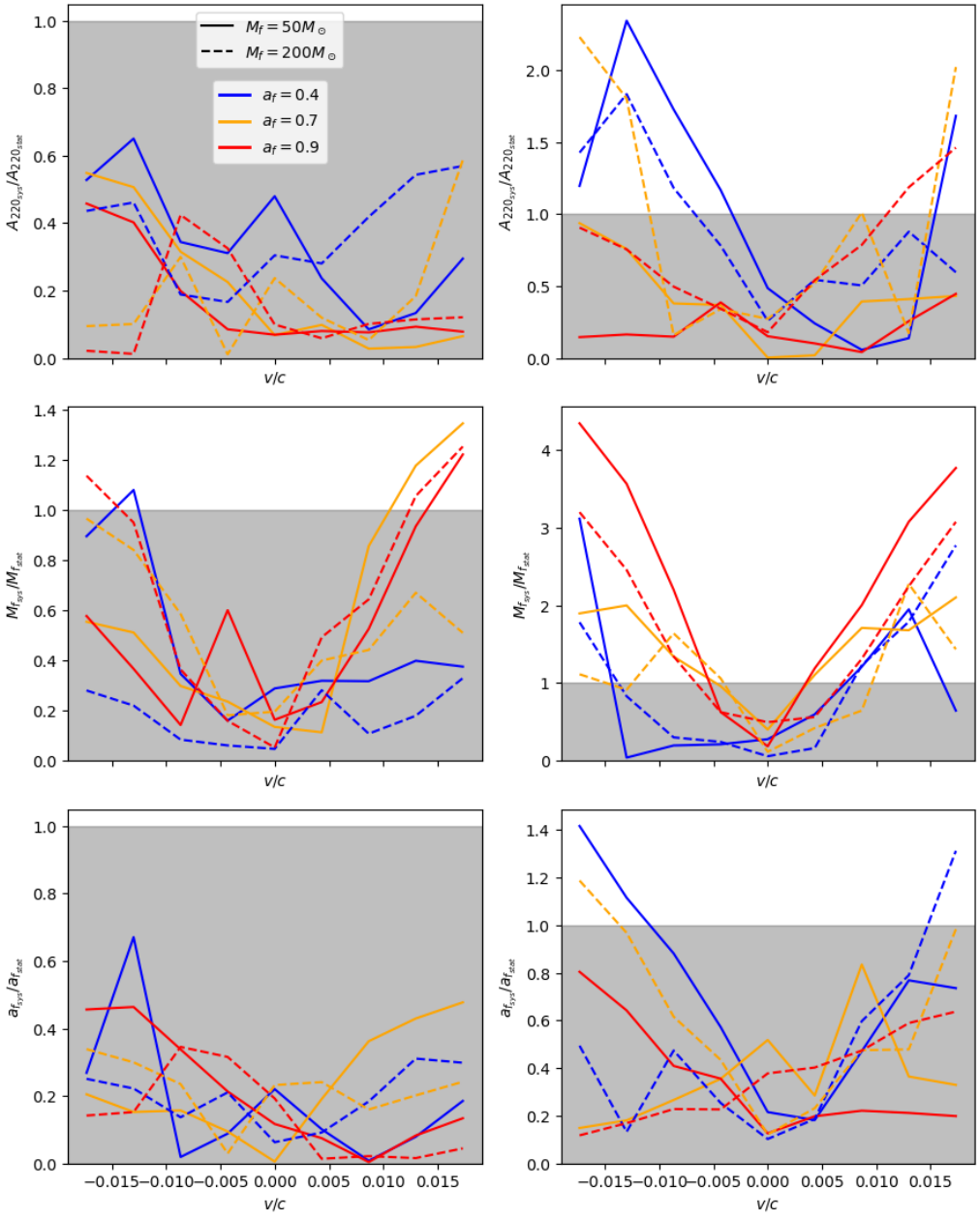

Figure 6.2: The ratios of systematic errors to the statistical errors of the amplitude, final mass and final spin for the model in Eqn. 6.1 in the top, middle and bottom rows respectively. Left (right) column shows the ratios for a network SNR of 50 (150). Line styles indicate the final mass of the system and the line colors indicate the final spin of the system in the legends of each plot. The shaded region indicates where the statistical error (1-σ error) is greater than the systematic error.

$M_f(M_\odot)$	a_f	ι	φ_0	α	δ	ψ	v_i	A_{330}/A_{220}	ϕ_{330}
50	0.9	$\pi/4$	0	2.25	-1.25	0	$0.01c$	0.3	0

Table 6.1: Injected parameter values for the injections to explore the detectability prospects. The angles are in radians and all the components of kick are the same ($v_x = v_y = v_z \equiv v_i$). The posteriors are plotted in Fig. 6.3 and 6.4.

with the ratios from Fig. 6.1. However, here we don't record any notable trends between different curves.

6.2 Detectability

Ref. [96] showed that aberration can, in principle, break the degeneracy between the mass and the kick. However, in the case of the aberrated ringdown model (Eqn. 3.20), unlike the Doppler shifted model, it is not straightforward to determine whether the kick remains degenerate with the mass. To investigate this issue, we resort to numerical calculations along with Bayesian parameter estimation techniques. Specifically, we compute the (22) mode in the observer frame numerically (Eqn. 3.21). As the fiducial signal model, we include only the dominant mode and the leading subdominant mode in the source frame as our true model (Eqn. 6.1). We inject the signal into Gaussian noise in a network of LIGO Hanford and Livingston detectors at their design sensitivities. The injected parameters are listed in table 6.1. We consider two cases where choose the amplitude and phase of the 220 mode by fixing the network SNR to 50 and 150.

Bayesian analysis being computationally expensive, we estimate only a subset of the injected parameters. We first keep the final mass, final spin, angle of inclination and the velocity components as the free parameters: $(M_f, a_f, \iota, v_x, v_y, v_z)$. We choose flat uniform priors over the final mass in the range $20 < M_f < 300$, final spin in the range $0.01 < a_f < 0.99$, inclination in the range $0 < \iota < \pi$ and velocity components in the range $-1 < v_i < 1$. In Fig. 6.3, we show the corner plot of the estimated parameters, including their one-dimensional marginalized and two-dimensional joint posterior distributions. All the parameters are recovered well–the injected values are within the $1-\sigma$ bounds from the median values of the parameters. We list the injected values, median values along with their upper and lower $1-\sigma$ bounds and maximum a-posteriori (MAP) values in table 6.2. The statistical errors decrease as we increase the network SNR. We further see that the recovery of the $x-$ and $y-$components of the velocity is better than the $z-$component. Apart from that, we would like to note another observation. Generally, when Bayesian parameter estimation is employed, a positive correlation between the final

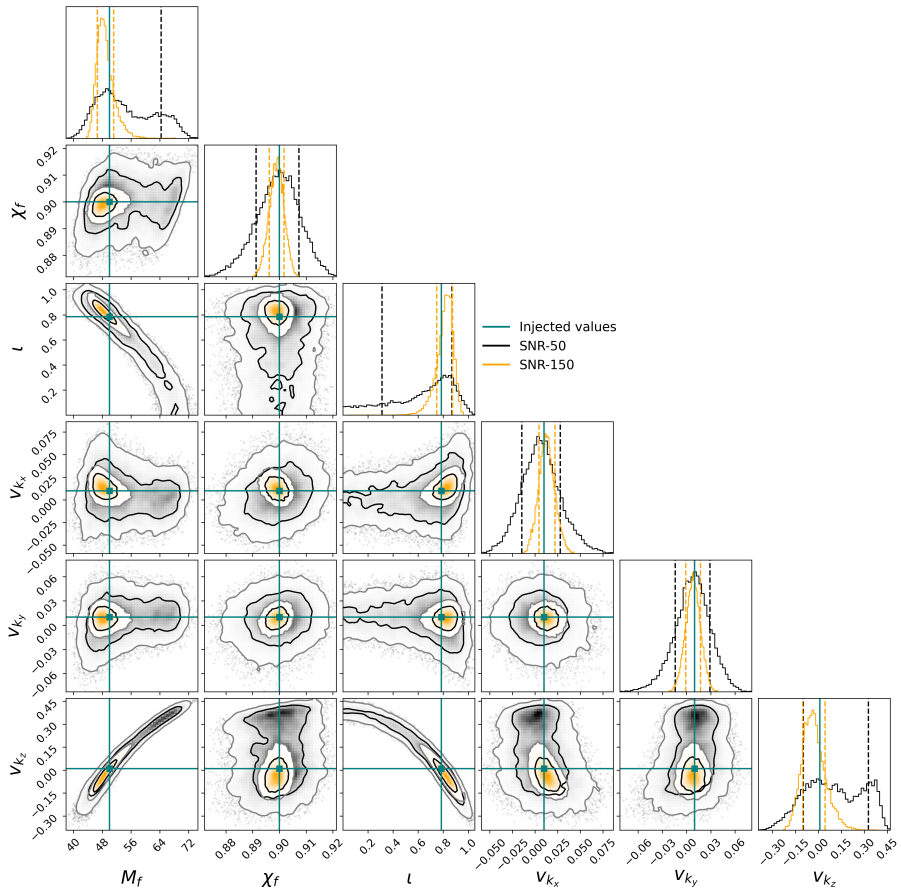

Figure 6.3: Posteriors for final mass M_f, final spin a_f, angle of inclination ι and the velocity (v_x, v_y, v_z). Teal lines represent the injected values. The contours show 68 % and 95 % credible regions in the 2D corner plots. The black color represents the SNR 50 case and orange color represents the SNR 150 case.

Parameter	Injected values	MAP values		Median values	
		SNR 50	SNR 150	SNR 50	SNR 150
$M_f(M_\odot)$	50	49.72	51.19	$52.99^{+11.38}_{-6.342}$	$48.71^{+3.767}_{-2.178}$
a_f	0.9	0.8987	0.8985	$0.8997^{+0.007530}_{-0.008471}$	$0.8990^{+0.003045}_{-0.003245}$
ι	$\pi/4$	0.7728	0.7539	$0.6968^{+0.1722}_{-0.3843}$	$0.8161^{+0.06152}_{-0.1019}$
v_{k_x}	0.01	0.008473	0.01422	$0.005986^{+0.02174}_{-0.02063}$	$0.01218^{+0.01051}_{-0.009979}$
v_{k_y}	0.01	0.1500	0.01943	$0.008358^{+0.02069}_{-0.02234}$	$0.007947^{+0.01047}_{-0.01046}$
v_{k_z}	0.01	0.6348	0.04425	$0.007488^{+0.2336}_{-0.1911}$	$-0.02984^{+0.1095}_{-0.07635}$

Table 6.2: Injected, maximum a-posteriori (MAP), and median posterior values shown in Fig. 6.3. The $\pm 1\sigma$ uncertainties are shown with the median values for network SNRs of 50 and 150.

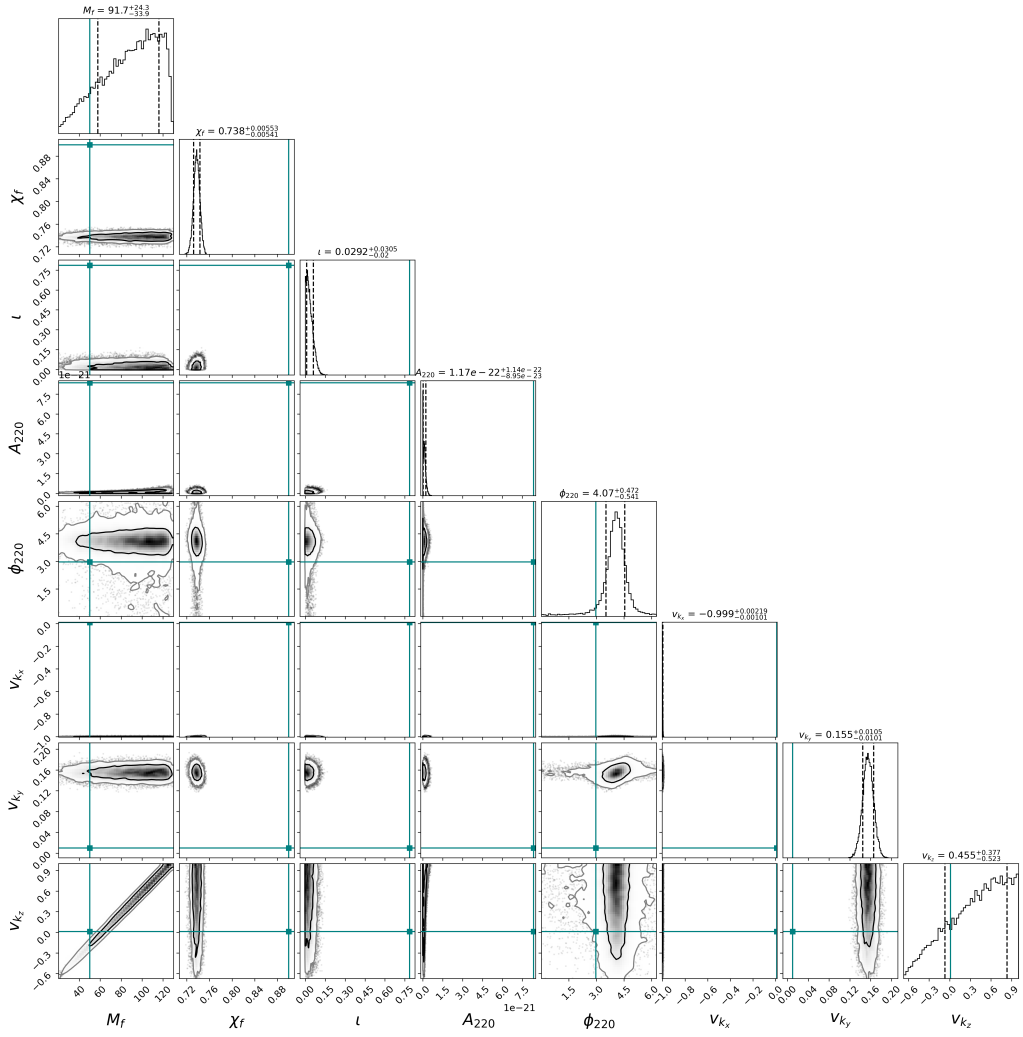

Figure 6.4: Posteriors for final mass M_f, final spin a_f, amplitude of the 220 mode A_{220}, phase of the 220 mode ϕ_{220}, angle of inclination ι and the velocity (v_x, v_y, v_z). Teal lines represent the injected values. The contours show 68 % and 95 % credible regions in the 2D corner plots.

mass and final spin is obtained. However, this correlation does not appear here. We don't have a clear explanation for this recovery.

We now perform a Bayesian analysis of the same setup but this time vary the amplitude and phase of the (220) mode. So now the varying parameters are $(M_f, a_f, A_{220}, \phi_{220}, \iota, v_x, v_y, v_z)$. We choose the same priors as the last parameter estimation run. We choose flat uniform prior for phase in the range $0 < \phi_{220} < 2\pi$ and a log uniform prior for the amplitude of the 220 mode in the range $-24 < \log A_{220} < -18$. We report the result in Fig. 6.4. In Fig. 6.4, we show the corner plot of the estimated parameters, including their one-dimensional marginalized and two-dimensional joint posterior distributions. We see a clear degeneracy between the mass and the $z-$component of the kick velocity in the lower left 2D corner plot. Along with this degeneracy, keeping the amplitude as free

Parameter	Injected values	MAP values	Median values
$M_f(M_\odot)$	50	104.9	$91.73^{+24.41}_{-34.06}$
a_f	0.9	0.7364	$0.7377^{+0.005556}_{-0.005447}$
ι	$\pi/4$	0.008247	$0.02918^{+0.03066}_{-0.02005}$
A_{220}	8.347×10^{-21}	2.065×10^{-22}	$1.173 \times 10^{-22+1.149\times10^{-22}}_{-8.989\times10^{-23}}$
ϕ_{220}	2.976	3.985	$4.068^{+0.4743}_{-0.5434}$
v_{k_x}	0.001	-0.999	$-0.9986^{+0.002205}_{-0.001018}$
v_{k_y}	0.001	0.15	$0.1550^{+0.01061}_{-0.01016}$
v_{k_z}	0.001	0.6348	$0.4553^{+0.3782}_{-0.5263}$

Table 6.3: The injected, maximum a-posteriori (MAP) and the median values of the posterior as shown in Fig. 6.4. The $\pm 1 - \sigma$ errors are also shown along with the median values.

parameter, for this model we see new degeneracies: amplitude A_{220} is degenerate with the $z-$component of the velocity v_z and the angle of inclination ι is degenerate with the $x-$component of the velocity v_x. Due to these degeneracies, we see that the recovery of all the other parameters is also affected. The median values along with their upper and lower 1-σ errors, maximum a-posteriori (MAP) values and the injected values are shown in table 6.3. This analysis shows that the detection of BH kick from ringdown analysis remains challenging.

In this chapter, we first looked at the systematic biases due to the aberration effect. Along with the bias in the final mass, we see a bias in the mode amplitude and the final spin. The bias in the amplitude arises due to the direct modification of the amplitude due to the aberration effect. The bias in the spin arises due to the change in the waveform frequency profile due to the addition of two damped sinusoids. We further explored the detectability prospects using Bayesian parameter estimation since commenting about the degeneracy is not trivial as was the case in Doppler shift. As an illustrative case, we take the model as given by Eqn. 6.1 and first vary the final mass, final spin, angle of inclination and the velocity components in the parameter estimation run. This analysis reveals that it is possible to break the degeneracy between mass and the kick and all the injected values are recovered within their $1 - \sigma$ bounds. We then perform a more general Bayesian analysis by varying the amplitude and the phase of the (220) mode along with other parameters. In this analysis, we see that the degeneracy between mass and kick velocity is retained. Along with that, we also encounter new degeneracies: amplitude A_{220} is degenerate with the $z-$component of the velocity v_z and the angle of inclination ι is degenerate with the $x-$component of the velocity v_x. We further plan to explore the recovery of the parameters by varying a single component of the velocity and study

the correlations between different parameters. This will be particularly useful for the 3G detectors as they are expected to see higher mass systems with higher SNRs.

Chapter 7

Conclusions and Outlook

In case of binary black hole mergers, gravitational radiation carries away not only energy and angular momentum but also linear momentum. The asymmetric emission of this linear momentum flux during the merger results in a recoil of the remnant black hole, commonly referred to as a black hole kick. The magnitude of this kick can reach several thousand kilometers per second depending on the masses and spins of the progenitor black holes.

To explore the effect of such a kick, ref. [81] modifies the nonprecessing phenomenological `IMRPhenomD` waveform, which splits the GW signal into three phases (inspiral, intermediate, and merger/ringdown) that are "stitched" together via step functions. The authors only modify the ringdown phase by replacing the real and imaginary components of the ringdown frequency: $(f_{RD}, f_{damp}) \rightarrow (f_{RD}, f_{damp})(1 + v_r)$. With this modified waveform they study the measurability of the kick imparted to the remnant black hole. However, ref. [75] shows that waveform models from different families show inconsistencies in their kick predictions when computed using the linear momentum flux hinting towards significant systematics between waveform models of different families.

In this thesis, we investigate the impact of the recoil velocities on the gravitational wave ringdown signal from binary black hole mergers. Since most of the kick is imparted close to the merger, we model its effect on the ringdown waveform by assuming a constant kick velocity of the remnant black hole during the ringdown phase. The motion of the remnant black hole relative to the observer introduces relativistic effects in the observed waveform, primarily in the form of Doppler shifts and aberration. Since the velocities are non-relativistic, we incorporate them in the non-relativisitic limit.

In chapter 3, we obtain the modified ringdown waveform due to the Doppler shift and aberration effect in their non-relativistic limits. In chapter 5, we start by looking at mismatches between Doppler shifted waveforms and non-Doppler shifted waveforms. This is done for three cases of ringdown models containing 1.) (220) mode only, 2.) (220,221) modes and (220,330) modes. This mismatch analysis overall shows that the mismatch between a Doppler shifted waveform and a non-Doppler shifted waveform is independent of the final mass and increases with increase in spin. This means that as long as the signal lies in the frequency band of the detector, for a particular SNR, it is the final spin and not the final mass that determines how different a kicked waveform will be from a one that is not kicked. The biases observed in the ringdown model with (220, 330) modes is almost always greater than the biases observed in the model with only the (220) mode which in turn is greater than the model with the (220, 221) modes. So the mismatch essentially is dictated by the lifetime of the most dominant ringdown mode.

To investigate the systematic biases, we further employ Bayesian analysis where we inject Doppler shifted waveforms in Gaussian noise and analyze them with non-Doppler shifted waveforms. Bias plots on the final mass and final spin show that the final mass is biased whereas the final spin is not. This is explained using the degeneracy between the final mass and kick velocity. The same trends which were seen in the mismatch plots were seen in the Bayesian analysis as well i.e. the ratio of the systematic error to the statistical error is independent of the mass and increases with increase in spin. For example, for $M_f = 50M_\odot, v_r/c = 0.015$ and SNR 100, the ratios of the systematic errors to the statistical errors are $\sim$[1.5, 1.5, 2.2, 3, 4.5] for final spins of $a_f = [0.4, 0.6, 0.8, 0.9, 0.95]$ respectively. Using a back-of-the-envelope argument, we also explored the detectability prospects of the kick assuming the final mass is estimated accurately using the inspiral. This analysis reveals that a kick of $0.01c$ could be measured at a network SNR of 80.

In chapter 6, we then investigate the effect of aberration in the ringdown model. Aberration introduces mode-mixing and corrections in the mode amplitudes in the ringdown model. Bayesian analysis reveals that along with final mass, the mode amplitudes and final spin are biased if non-aberrated non-Doppler shifted model is used to analyze aberrated Doppler shifted model. We then perform Bayesian analysis to investigate the detectability prospects for a chosen aberrated model. We vary the final mass, final spin, angle of inclination and the three components of velocity and see that the degeneracy of the final mass and kick is broken. The injected values are recovered within the $1-\sigma$ bounds for all the parameters. We note that the transverse components (x and y) of the velocity are recovered better than the z component of the velocity. For a network SNR of 150, $v_x \neq 0$ is measured with $1-\sigma$ confidence.

We than perform a more general analysis of the same setup by keeping the amplitude

and the phase of the (220) mode as free parameters along with the aforementioned parameters. We see that new degeneracies are introduced in this general setup: amplitude A_{220} is degenerate with the $z-$component of the velocity v_z and the angle of inclination ι is degenerate with the $x-$component of the velocity v_z. These new degeneracies affect the recovery of all the parameters and none of the parameters are recovered well.

As a key objective for the future, to further investigate the detectability prospects of the kick velocity observed in Chapter 6, it would be useful to first consider a more restricted model with fewer free parameters. In particular, we plan to set two components of the kick velocity to zero and retain only one non-zero component, and then study the recovery of this parameter. We also plan to incorporate inspiral-informed priors on the remnant mass, spin, and amplitude when estimating the kick velocity. Finally, measuring the kick would be particularly promising for observations with next-generation GW detectors, where higher signal-to-noise ratios are expected to provide tighter constraints and more accurate estimates of the recoil velocity.

Bibliography

[1] R. A. Hulse and J. H. Taylor. Discovery of a pulsar in a binary system. , 195: L51–L53, January 1975. doi: 10.1086/181708.

[2] J Aasi et al. Advanced ligo. Classical and Quantum Gravity, 32(7):074001, March 2015. ISSN 1361-6382. doi: 10.1088/0264-9381/32/7/074001. URL http://dx.doi.org/10.1088/0264-9381/32/7/074001.

[3] B.P. Abbott et al. Gw150914: First results from the search for binary black hole coalescence with advanced ligo. Physical Review D, 93(12), June 2016. ISSN 2470-0029. doi: 10.1103/physrevd.93.122003. URL http://dx.doi.org/10.1103/PhysRevD.93.122003.

[4] The LIGO Scientific Collaboration et al. Gwtc-4.0: An introduction to version 4.0 of the gravitational-wave transient catalog, 2025. URL https://arxiv.org/abs/2508.18080.

[5] The LIGO Scientific Collaboration et al. Gwtc-4.0: Updating the gravitational-wave transient catalog with observations from the first part of the fourth ligo-virgo-kagra observing run, 2025. URL https://arxiv.org/abs/2508.18082.

[6] N. V. Krishnendu and Frank Ohme. Testing general relativity with gravitational waves: An overview. Universe, 7(12):497, December 2021. ISSN 2218-1997. doi: 10.3390/universe7120497. URL http://dx.doi.org/10.3390/universe7120497.

[7] B. P. Abbott et al. Binary black hole population properties inferred from the first and second observing runs of advanced ligo and advanced virgo. The Astrophysical Journal Letters, 882(2):L24, September 2019. ISSN 2041-8213. doi: 10.3847/2041-8213/ab3800. URL http://dx.doi.org/10.3847/2041-8213/ab3800.

[8] B. P. Abbott et al. Binary black hole mergers in the first advanced ligo observing run. Phys. Rev. X, 6:041015, Oct 2016. doi: 10.1103/PhysRevX.6.041015. URL https://link.aps.org/doi/10.1103/PhysRevX.6.041015.

[9] R. Abbott et al. Population properties of compact objects from the second ligo–virgo gravitational-wave transient catalog. The Astrophysical Journal Letters, 913(1):L7, May 2021. ISSN 2041-8213. doi: 10.3847/2041-8213/abe949. URL http://dx.doi.org/10.3847/2041-8213/abe949.

[10] R. Abbott et al. Population of merging compact binaries inferred using gravitational waves through gwtc-3. Physical Review X, 13(1), March 2023. ISSN 2160-3308. doi: 10.1103/physrevx.13.011048. URL http://dx.doi.org/10.1103/PhysRevX.13.011048.

[11] The LIGO Scientific Collaboration et al. Gwtc-4.0: Population properties of merging compact binaries, 2025. URL https://arxiv.org/abs/2508.18083.

[12] Simone Mastrogiovanni, Astrid Lamberts, Rahul Srinivasan, Tristan Bruel, and Nelson Christensen. Inferring binary black holes stellar progenitors with gravitational wave sources. Mon. Not. Roy. Astron. Soc., 517(3):3432–3444, 2022. doi: 10.1093/mnras/stac2850.

[13] Kaze W. K. Wong, Katelyn Breivik, Will M. Farr, and Rodrigo Luger. Backward population synthesis: Mapping the evolutionary history of gravitational-wave progenitors. The Astrophysical Journal, 950(2):181, June 2023. ISSN 1538-4357. doi: 10.3847/1538-4357/acc863. URL http://dx.doi.org/10.3847/1538-4357/acc863.

[14] Konstantin A. Postnov and Lev R. Yungelson. The evolution of compact binary star systems. Living Reviews in Relativity, 17(1), May 2014. ISSN 1433-8351. doi: 10.12942/lrr-2014-3. URL http://dx.doi.org/10.12942/lrr-2014-3.

[15] Matthias U. Kruckow, Thomas M. Tauris, Norbert Langer, Michael Kramer, and Robert G. Izzard. Progenitors of gravitational wave mergers: binary evolution with the stellar grid-based code COMBINE. , 481(2):1908–1949, December 2018. doi: 10.1093/mnras/sty2190.

[16] Jeff Riley et al. Rapid stellar and binary population synthesis with compas. The Astrophysical Journal Supplement Series, 258(2):34, February 2022. ISSN 1538-4365. doi: 10.3847/1538-4365/ac416c. URL http://dx.doi.org/10.3847/1538-4365/ac416c.

[17] Marc Favata. The gravitational-wave memory effect. Class. Quant. Grav., 27: 084036, 2010. doi: 10.1088/0264-9381/27/8/084036.

[18] P. Polunin, Y. Yang, J. Atalaya, E. Ng, S. Strachan, O. Shoshani, M. Dykman, S. Shaw, and T. Kenny. Characterizing mems nonlinearities directly: The ringdown measurements. In 2015 Transducers - 2015 18th International Conference on Solid-State Sensors, Actuators and Microsystems (TRANSDUCERS), pages 2176–2179, 2015. doi: 10.1109/TRANSDUCERS.2015.7181391.

[19] Yi Qiu, Xisco Jiménez Forteza, and Pierre Mourier. Linear versus nonlinear modeling of black hole ringdowns. Phys. Rev. D, 109:064075, Mar 2024. doi: 10.1103/PhysRevD.109.064075. URL https://link.aps.org/doi/10.1103/PhysRevD.109.064075.

[20] D. Perrone, T. Barreira, A. Kehagias, and A. Riotto. Non-linear black hole ringdowns: An analytical approach. Nuclear Physics B, 999:116432, February 2024. ISSN 0550-3213. doi: 10.1016/j.nuclphysb.2023.116432. URL http://dx.doi.org/10.1016/j.nuclphysb.2023.116432.

[21] Taillte May, Sizheng Ma, Justin L. Ripley, and William E. East. Nonlinear effect of absorption on the ringdown of a spinning black hole. Phys. Rev. D, 110:084034, Oct 2024. doi: 10.1103/PhysRevD.110.084034. URL https://link.aps.org/doi/10.1103/PhysRevD.110.084034.

[22] A. Kehagias and A. Riotto. Nonlinear effects in black hole ringdown made simple: Quasi-normal modes as adiabatic modes, 2024. URL https://arxiv.org/abs/2411.07980.

[23] Laura Sberna, Pablo Bosch, William E. East, Stephen R. Green, and Luis Lehner. Nonlinear effects in the black hole ringdown: Absorption-induced mode excitation. , 105(6):064046, March 2022. doi: 10.1103/PhysRevD.105.064046.

[24] Neev Khera, Ariadna Ribes Metidieri, Béatrice Bonga, Xisco Jiménez Forteza, Badri Krishnan, Eric Poisson, Daniel Pook-Kolb, Erik Schnetter, and Huan Yang. Nonlinear ringdown at the black hole horizon. Phys. Rev. Lett., 131:231401, Dec 2023. doi: 10.1103/PhysRevLett.131.231401. URL https://link.aps.org/doi/10.1103/PhysRevLett.131.231401.

[25] Keefe Mitman, Macarena Lagos, Leo C. Stein, Sizheng Ma, Lam Hui, Yanbei Chen, Nils Deppe, Fran çois Hébert, Lawrence E. Kidder, Jordan Moxon, Mark A. Scheel, Saul A. Teukolsky, William Throwe, and Nils L. Vu. Nonlinearities in black hole ringdowns. Phys. Rev. Lett., 130:081402, Feb 2023. doi: 10.1103/PhysRevLett.130.081402. URL https://link.aps.org/doi/10.1103/PhysRevLett.130.081402.

[26] Ian Hinder, Birjoo Vaishnav, Frank Herrmann, Deirdre M. Shoemaker, and Pablo Laguna. Circularization and final spin in eccentric binary-black-hole inspirals. Physical Review D, 77(8), April 2008. ISSN 1550-2368. doi: 10.1103/physrevd.77.081502. URL http://dx.doi.org/10.1103/PhysRevD.77.081502.

[27] P. C. Peters and J. Mathews. Gravitational radiation from point masses in a keplerian orbit. Phys. Rev., 131:435–440, Jul 1963. doi: 10.1103/PhysRev.131.435. URL https://link.aps.org/doi/10.1103/PhysRev.131.435.

[28] B. P. Abbott et al. Search for eccentric binary black hole mergers with advanced ligo and advanced virgo during their first and second observing runs. The Astrophysical Journal, 883(2):149, September 2019. ISSN 1538-4357. doi: 10.3847/1538-4357/ab3c2d. URL http://dx.doi.org/10.3847/1538-4357/ab3c2d.

[29] The LIGO Scientific Collaboration et al. Search for eccentric black hole coalescences during the third observing run of ligo and virgo, 2023. URL https://arxiv.org/abs/2308.03822.

[30] Yi-Fan Wang and Alexander H. Nitz. Search for gravitational waves from eccentric binary black holes with an effective-one-body template. The Astrophysical Journal, 993(2):215, November 2025. ISSN 1538-4357. doi: 10.3847/1538-4357/ae0f1b. URL http://dx.doi.org/10.3847/1538-4357/ae0f1b.

[31] A. G. Abac et al. Black Hole Spectroscopy and Tests of General Relativity with GW250114. Phys. Rev. Lett., 136(4):041403, 2026. doi: 10.1103/6c61-fm1n.

[32] A. G. Abac et al. Gw250114: Testing hawking's area law and the kerr nature of black holes. Phys. Rev. Lett., 135:111403, Sep 2025. doi: 10.1103/kw5g-d732. URL https://link.aps.org/doi/10.1103/kw5g-d732.

[33] Neil Lu, Sizheng Ma, Ornella J. Piccinni, Yanbei Chen, and Ling Sun. Gw250114 reveals black hole horizon signatures, 2025. URL https://arxiv.org/abs/2510.01001.

[34] W. B. Bonnor and M. A. Rotenberg. Transport of Momentum by Gravitational Waves: The Linear Approximation. Proceedings of the Royal Society of London Series A, 265(1320):109–116, December 1961. doi: 10.1098/rspa.1961.0226.

[35] Asher Peres. Classical radiation recoil. Phys. Rev., 128:2471–2475, Dec 1962. doi: 10.1103/PhysRev.128.2471. URL https://link.aps.org/doi/10.1103/PhysRev.128.2471.

[36] Jacob D. Bekenstein. Gravitational-Radiation Recoil and Runaway Black Holes. , 183:657–664, July 1973. doi: 10.1086/152255.

[37] M. J. Fitchett. The influence of gravitational wave momentum losses on the centre of mass motion of a Newtonian binay system. , 203:1049–1062, June 1983. doi: 10.1093/mnras/203.4.1049.

[38] Luc Blanchet, Moh'd S. S. Qusailah, and Clifford M. Will. Gravitational recoil of inspiraling black hole binaries to second post-newtonian order. The Astrophysical Journal, 635(1):508, dec 2005. doi: 10.1086/497332. URL https://doi.org/10.1086/497332.

[39] Thibault Damour and Achamveedu Gopakumar. Gravitational recoil during binary black hole coalescence using the effective one body approach. Phys. Rev. D, 73: 124006, Jun 2006. doi: 10.1103/PhysRevD.73.124006. URL https://link.aps.org/doi/10.1103/PhysRevD.73.124006.

[40] Carlos O. Lousto and Yosef Zlochower. Further insight into gravitational recoil. Phys. Rev. D, 77:044028, Feb 2008. doi: 10.1103/PhysRevD.77.044028. URL https://link.aps.org/doi/10.1103/PhysRevD.77.044028.

[41] José A. González, Ulrich Sperhake, Bernd Brügmann, Mark Hannam, and Sascha Husa. Maximum kick from nonspinning black-hole binary inspiral. Phys. Rev. Lett., 98:091101, Feb 2007. doi: 10.1103/PhysRevLett.98.091101. URL https://link.aps.org/doi/10.1103/PhysRevLett.98.091101.

[42] Alexandre Le Tiec, Luc Blanchet, and Clifford M Will. The gravitational-wave recoil from the ringdown phase of coalescing black hole binaries. Classical and Quantum Gravity, 27(1):012001, dec 2009. doi: 10.1088/0264-9381/27/1/012001. URL https://doi.org/10.1088/0264-9381/27/1/012001.

[43] Carlos O. Lousto, Yosef Zlochower, Massimo Dotti, and Marta Volonteri. Gravitational recoil from accretion-aligned black-hole binaries. Phys. Rev. D, 85:084015, Apr 2012. doi: 10.1103/PhysRevD.85.084015. URL https://link.aps.org/doi/10.1103/PhysRevD.85.084015.

[44] Carlos O. Lousto and Yosef Zlochower. Nonlinear gravitational recoil from the mergers of precessing black-hole binaries. Phys. Rev. D, 87:084027, Apr 2013. doi: 10.1103/PhysRevD.87.084027. URL https://link.aps.org/doi/10.1103/PhysRevD.87.084027.

[45] Parthapratim Mahapatra, Anuradha Gupta, Marc Favata, K. G. Arun, and B. S. Sathyaprakash. Remnant black hole kicks and implications for hierarchical mergers. The Astrophysical Journal Letters, 918(2):L31, September 2021. ISSN 2041-8213. doi: 10.3847/2041-8213/ac20db. URL http://dx.doi.org/10.3847/2041-8213/ac20db.

[46] Vijay Varma, Sylvia Biscoveanu, Tousif Islam, Feroz H. Shaik, Carl-Johan Haster, Maximiliano Isi, Will M. Farr, Scott E. Field, and Salvatore Vitale. Evidence of large recoil velocity from a black hole merger signal. Physical Review Letters, 128 (19), May 2022. ISSN 1079-7114. doi: 10.1103/physrevlett.128.191102. URL http://dx.doi.org/10.1103/PhysRevLett.128.191102.

[47] Manuela Campanelli, Carlos O. Lousto, Yosef Zlochower, and David Merritt. Maximum gravitational recoil. Phys. Rev. Lett., 98:231102, Jun 2007. doi:

10.1103/PhysRevLett.98.231102. URL https://link.aps.org/doi/10.1103/PhysRevLett.98.231102.

[48] Wolfgang Tichy and Pedro Marronetti. Binary black hole mergers: Large kicks for generic spin orientations. Phys. Rev. D, 76:061502, Sep 2007. doi: 10.1103/PhysRevD.76.061502. URL https://link.aps.org/doi/10.1103/PhysRevD.76.061502.

[49] José A. González, Mark Hannam, Ulrich Sperhake, Bernd Brügmann, and Sascha Husa. Supermassive recoil velocities for binary black-hole mergers with antialigned spins. Phys. Rev. Lett., 98:231101, Jun 2007. doi: 10.1103/PhysRevLett.98.231101. URL https://link.aps.org/doi/10.1103/PhysRevLett.98.231101.

[50] Carlos O. Lousto and Yosef Zlochower. Hangup kicks: Still larger recoils by partial spin-orbit alignment of black-hole binaries. Phys. Rev. Lett., 107:231102, Dec 2011. doi: 10.1103/PhysRevLett.107.231102. URL https://link.aps.org/doi/10.1103/PhysRevLett.107.231102.

[51] Carlos O. Lousto and James Healy. Kicking gravitational wave detectors with recoiling black holes. Phys. Rev. D, 100:104039, Nov 2019. doi: 10.1103/PhysRevD.100.104039. URL https://link.aps.org/doi/10.1103/PhysRevD.100.104039.

[52] Ulrich Sperhake, Roxana Rosca-Mead, Davide Gerosa, and Emanuele Berti. Amplification of superkicks in black-hole binaries through orbital eccentricity. Phys. Rev. D, 101:024044, Jan 2020. doi: 10.1103/PhysRevD.101.024044. URL https://link.aps.org/doi/10.1103/PhysRevD.101.024044.

[53] Fabio Antonini and Frederic A. Rasio. Merging Black Hole Binaries in Galactic Nuclei: Implications for Advanced-LIGO Detections. , 831(2):187, November 2016. doi: 10.3847/0004-637X/831/2/187.

[54] David Merritt, Milo Milosavljevi, Marc Favata, Scott A. Hughes, and Daniel E. Holz. Consequences of gravitational radiation recoil. The Astrophysical Journal, 607(1):L9–L12, April 2004. ISSN 1538-4357. doi: 10.1086/421551. URL http://dx.doi.org/10.1086/421551.

[55] Noam I. Libeskind, Shaun Cole, Carlos S. Frenk, and John C. Helly. The effect of gravitational recoil on black holes forming in a hierarchical universe. , 368(3):1381–1391, May 2006. doi: 10.1111/j.1365-2966.2006.10209.x.

[56] Davide Gerosa and Emanuele Berti. Are merging black holes born from stellar collapse or previous mergers? Phys. Rev. D, 95:124046, Jun 2017. doi: 10.1103/PhysRevD.95.124046. URL https://link.aps.org/doi/10.1103/PhysRevD.95.124046.

[57] Zoheyr Doctor, Ben Farr, and Daniel E. Holz. Black hole leftovers: The remnant population from binary black hole mergers. The Astrophysical Journal Letters, 914 (1):L18, jun 2021. doi: 10.3847/2041-8213/ac0334. URL https://doi.org/10.3847/2041-8213/ac0334.

[58] Carlos Araújo-Álvarez, Henry W. Y. Wong, Anna Liu, and Juan Calderón Bustillo. Kicking time back in black hole mergers: Ancestral masses, spins, birth recoils, and hierarchical-formation viability of gw190521. The Astrophysical Journal, 977(2): 220, dec 2024. doi: 10.3847/1538-4357/ad90a9. URL https://doi.org/10.3847/1538-4357/ad90a9.

[59] Parthapratim Mahapatra, Debatri Chattopadhyay, Anuradha Gupta, Fabio Antonini, Marc Favata, B. S. Sathyaprakash, and K. G. Arun. Reconstructing the genealogy of ligo-virgo black holes. The Astrophysical Journal, 975(1):117, oct 2024. doi: 10.3847/1538-4357/ad781b. URL https://doi.org/10.3847/1538-4357/ad781b.

[60] I. H. Redmount and M. J. Rees. Gravitational-radiation rocket effects and galactic structure. Comments on Astrophysics, 14:165, January 1989.

[61] Alberto Sesana. Extreme recoils: impact on the detection of gravitational waves from massive black hole binaries. Monthly Notices of the Royal Astronomical Society: Letters, 382(1):L6–L10, November 2007. ISSN 1745-3933. doi: 10.1111/j.1745-3933.2007.00375.x. URL http://dx.doi.org/10.1111/j.1745-3933.2007.00375.x.

[62] Marta Volonteri, Kayhan Gültekin, and Massimo Dotti. Gravitational recoil: effects on massive black hole occupation fraction over cosmic time. Monthly Notices of the Royal Astronomical Society, March 2010. ISSN 1365-2966. doi: 10.1111/j.1365-2966.2010.16431.x. URL http://dx.doi.org/10.1111/j.1365-2966.2010.16431.x.

[63] Piero Madau and Eliot Quataert. The effect of gravitational-wave recoil on the demography of massive black holes. Astrophysical Journal, 606(1 II):L17–L20, May 2004. ISSN 0004-637X. doi: 10.1086/421017.

[64] Abraham Loeb. Observable signatures of a black hole ejected by gravitational-radiation recoil in a galaxy merger. Phys. Rev. Lett., 99:041103, Jul 2007. doi: 10.1103/PhysRevLett.99.041103. URL https://link.aps.org/doi/10.1103/PhysRevLett.99.041103.

[65] S. Komossa and David Merritt. Gravitational wave recoil oscillations of black holes: Implications for unified models of active galactic nuclei. The Astrophysical Journal,

689(2):L89–L92, November 2008. ISSN 1538-4357. doi: 10.1086/595883. URL http://dx.doi.org/10.1086/595883.

[66] Alessia Gualandris and David Merritt. Ejection of supermassive black holes from galaxy cores. The Astrophysical Journal, 678(2):780, may 2008. doi: 10.1086/586877. URL https://doi.org/10.1086/586877.

[67] Laura Blecha and Abraham Loeb. Effects of gravitational-wave recoil on the dynamics and growth of supermassive black holes. Monthly Notices of the Royal Astronomical Society, October 2008. ISSN 1365-2966. doi: 10.1111/j.1365-2966.2008.13790.x. URL http://dx.doi.org/10.1111/j.1365-2966.2008.13790.x.

[68] Marta Volonteri and Piero Madau. Off-nuclear agns as a signature of recoiling massive black holes. The Astrophysical Journal, 687(2):L57–L60, October 2008. ISSN 1538-4357. doi: 10.1086/593353. URL http://dx.doi.org/10.1086/593353.

[69] F. K. Liu, Dong Wang, and Xian Chen. Recoiling supermassive black holes in spin-flip radio galaxies. The Astrophysical Journal, 746(2):176, February 2012. ISSN 1538-4357. doi: 10.1088/0004-637x/746/2/176. URL http://dx.doi.org/10.1088/0004-637X/746/2/176.

[70] Marco Chiaberge, Takahiro Morishita, Matteo Boschini, Stefano Bianchi, Alessandro Capetti, Gianluca Castignani, Davide Gerosa, Masahiro Konishi, Shuhei Koyama, Kosuke Kushibiki, Erini Lambrides, Eileen T. Meyer, Kentaro Motohara, Massimo Stiavelli, Hidenori Takahashi, Grant R. Tremblay, and Colin Norman. A recoiling supermassive black hole in a powerful quasar, 2025. URL https://arxiv.org/abs/2501.18730.

[71] S. Komossa. Recoiling black holes: Electromagnetic signatures, candidates, and astrophysical implications. Advances in Astronomy, 2012:1–8, 2012. ISSN 1687-7977. doi: 10.1155/2012/364973. URL http://dx.doi.org/10.1155/2012/364973.

[72] Tamara Bogdanović, M. Coleman Miller, and Laura Blecha. Electromagnetic counterparts to massive black-hole mergers. Living Reviews in Relativity, 25 (1), June 2022. ISSN 1433-8351. doi: 10.1007/s41114-022-00037-8. URL http://dx.doi.org/10.1007/s41114-022-00037-8.

[73] M. Dotti, C. Montuori, R. Decarli, M. Volonteri, M. Colpi, and F. Haardt. Sdssj092712.65+294344.0: a candidate massive black hole binary. Monthly Notices of the Royal Astronomical Society: Letters, 398(1):L73–L77, September 2009. ISSN

1745-3925. doi: 10.1111/j.1745-3933.2009.00714.x. URL http://dx.doi.org/10.1111/j.1745-3933.2009.00714.x.

[74] Junyao Li, Ming-Yang Zhuang, and Yue Shen. Jwst confirms the nature of cid-42. The Astrophysical Journal, 961(1):19, jan 2024. doi: 10.3847/1538-4357/ad0e0d. URL https://doi.org/10.3847/1538-4357/ad0e0d.

[75] Angela Borchers and Frank Ohme. Inconsistent black hole kick estimates from gravitational-wave models. Classical and Quantum Gravity, 40(9):095008, April 2023. ISSN 1361-6382. doi: 10.1088/1361-6382/acc5da. URL http://dx.doi.org/10.1088/1361-6382/acc5da.

[76] Angela Borchers, Frank Ohme, Jannik Mielke, and Shrobana Ghosh. Observability of spin precession in the presence of a black-hole remnant kick. Physical Review D, 110(2), July 2024. ISSN 2470-0029. doi: 10.1103/physrevd.110.024037. URL http://dx.doi.org/10.1103/PhysRevD.110.024037.

[77] Jannik Mielke, Shrobana Ghosh, Angela Borchers, and Frank Ohme. Revisiting the relationship of black-hole kicks and multipole asymmetries. Physical Review D, 111(6), March 2025. ISSN 2470-0029. doi: 10.1103/physrevd.111.064009. URL http://dx.doi.org/10.1103/PhysRevD.111.064009.

[78] Jannik Mielke, Angela Borchers, and Frank Ohme. Uncovering subdominant multipole asymmetries in binary black-hole mergers, 2026. URL https://arxiv.org/abs/2602.17343.

[79] Manuela Campanelli, Carlos Lousto, Yosef Zlochower, and David Merritt. Large merger recoils and spin flips from generic black hole binaries. The Astrophysical Journal, 659(1):L5, mar 2007. doi: 10.1086/516712. URL https://doi.org/10.1086/516712.

[80] Davide Gerosa and Christopher J. Moore. Black hole kicks as new gravitational wave observables. Physical Review Letters, 117(1), June 2016. ISSN 1079-7114. doi: 10.1103/physrevlett.117.011101. URL http://dx.doi.org/10.1103/PhysRevLett.117.011101.

[81] Parthapratim Mahapatra, Marc Favata, and K. G. Arun. Testing general relativity via direct measurement of black hole kicks. Phys. Rev. D, 110(8):084041, 2024. doi: 10.1103/PhysRevD.110.084041.

[82] Juan Calderón Bustillo, James A. Clark, Pablo Laguna, and Deirdre Shoemaker. Tracking black hole kicks from gravitational-wave observations. Phys. Rev. Lett., 121:191102, Nov 2018. doi: 10.1103/PhysRevLett.121.191102. URL https://link.aps.org/doi/10.1103/PhysRevLett.121.191102.

[83] Vijay Varma, Scott E. Field, Mark A. Scheel, Jonathan Blackman, Davide Gerosa, Leo C. Stein, Lawrence E. Kidder, and Harald P. Pfeiffer. Surrogate models for precessing binary black hole simulations with unequal masses. Phys. Rev. Res., 1:033015, Oct 2019. doi: 10.1103/PhysRevResearch.1.033015. URL https://link.aps.org/doi/10.1103/PhysRevResearch.1.033015.

[84] Vijay Varma, Davide Gerosa, Leo C. Stein, François Hébert, and Hao Zhang. High-accuracy mass, spin, and recoil predictions of generic black-hole merger remnants. Physical Review Letters, 122(1), January 2019. ISSN 1079-7114. doi: 10.1103/physrevlett.122.011101. URL http://dx.doi.org/10.1103/PhysRevLett.122.011101.

[85] Tousif Islam, Scott E. Field, and Gaurav Khanna. Remnant black hole properties from numerical-relativity-informed perturbation theory and implications for waveform modelling, 2023. URL https://arxiv.org/abs/2301.07215.

[86] Tousif Islam and Digvijay Wadekar. Accurate models for recoil velocity distribution in black hole mergers with comparable to extreme mass-ratios and their astrophysical implications, 2025. URL https://arxiv.org/abs/2511.11536.

[87] Juan Calderón Bustillo, Samson H. W. Leong, and Koustav Chandra. A complete measurement of a black-hole recoil through higher-order gravitational-wave modes. Nature Astronomy, 9(10):1530–1540, September 2025. ISSN 2397-3366. doi: 10.1038/s41550-025-02632-5. URL http://dx.doi.org/10.1038/s41550-025-02632-5.

[88] Milton Ruiz, Miguel Alcubierre, Darío Núñez, and Ryoji Takahashi. Multiple expansions for energy and momenta carried by gravitational waves. General Relativity and Gravitation, 40(8):1705–1729, December 2007. ISSN 1572-9532. doi: 10.1007/s10714-007-0570-8. URL http://dx.doi.org/10.1007/s10714-007-0570-8.

[89] Davide Gerosa, François Hébert, and Leo C. Stein. Black-hole kicks from numerical-relativity surrogate models. Physical Review D, 97(10), May 2018. ISSN 2470-0029. doi: 10.1103/physrevd.97.104049. URL http://dx.doi.org/10.1103/PhysRevD.97.104049.

[90] Luciano Rezzolla, Rodrigo P. Macedo, and Jose Luis Jaramillo. Understanding the 'anti-kick' in the merger of binary black holes. Phys. Rev. Lett., 104:221101, 2010. doi: 10.1103/PhysRevLett.104.221101.

[91] Dae-Il Choi, Bernard J. Kelly, William D. Boggs, John G. Baker, Joan Centrella, and James van Meter. Recoiling from a kick in the head-on collision of spinning black holes. Physical Review D, 76(10), November 2007. ISSN 1550-2368. doi:

10.1103/physrevd.76.104026. URL http://dx.doi.org/10.1103/PhysRevD.76.104026.

[92] Sergio Dain, Carlos O. Lousto, and Yosef Zlochower. Extra-large remnant recoil velocities and spins from near-extremal-bowen-york-spin black-hole binaries. Physical Review D, 78(2), July 2008. ISSN 1550-2368. doi: 10.1103/physrevd.78.024039. URL http://dx.doi.org/10.1103/PhysRevD.78.024039.

[93] Bernd Brügmann, José A. González, Mark Hannam, Sascha Husa, and Ulrich Sperhake. Exploring black hole superkicks. Physical Review D, 77(12), June 2008. ISSN 1550-2368. doi: 10.1103/physrevd.77.124047. URL http://dx.doi.org/10.1103/PhysRevD.77.124047.

[94] James Healy and Carlos O. Lousto. Ultimate black hole recoil: What the maximum high energy collisions kick is?, 2024. URL https://arxiv.org/abs/2301.00018.

[95] Curt Cutler and Éanna E. Flanagan. Gravitational waves from merging compact binaries: How accurately can one extract the binary's parameters from the inspiral waveform? Physical Review D, 49(6):2658–2697, March 1994. ISSN 0556-2821. doi: 10.1103/physrevd.49.2658. URL http://dx.doi.org/10.1103/PhysRevD.49.2658.

[96] Alejandro Torres-Orjuela, Xian Chen, and Pau Amaro Seoane. Excitation of gravitational wave modes by a center-of-mass velocity of the source. Phys. Rev. D, 104 (12):123025, 2021. doi: 10.1103/PhysRevD.104.123025.

[97] Alejandro Torres-Orjuela, Pau Amaro Seoane, Zeyuan Xuan, Alvin J. K. Chua, María J. B. Rosell, and Xian Chen. Exciting Modes due to the Aberration of Gravitational Waves: Measurability for Extreme-Mass-Ratio Inspirals. Phys. Rev. Lett., 127(4):041102, 2021. doi: 10.1103/PhysRevLett.127.041102.

[98] Asad Ali, Salman Ahmad, M. Nawaz, Saleem Ullah, and Muhammad Aqeel. Bayesian inference on gravitational waves. Pakistan Journal of Statistics and Operation Research, 11:645, 12 2015. doi: 10.18187/pjsor.v11i4.1053.

[99] Gerson R. Santos, Antonio de Pádua Santos, Pavlos Protopapas, and Tiago A. E. Ferreira. Gravitational wave signal recognition and ring-down time estimation via artificial neural networks. Expert Systems with Applications, 207:117931, 2022. doi: 10.1016/j.eswa.2022.117931. URL https://doi.org/10.1016/j.eswa.2022.117931.

[100] Edward W. Leaver. Spectral decomposition of the perturbation response of the schwarzschild geometry. Phys. Rev. D, 34:384–408, Jul 1986. doi: 10.1103/PhysRevD.34.384. URL https://link.aps.org/doi/10.1103/PhysRevD.34.384.

[101] Emanuele Berti et al. Black hole spectroscopy: from theory to experiment, 2025. URL https://arxiv.org/abs/2505.23895.

[102] Eliot Finch. Black-hole Ringdown: Quasinormal Modes in Numerical-relativity Simulations and G PhD thesis, Birmingham U., 2023.

[103] Emanuele Berti, Vitor Cardoso, and Clifford M. Will. Gravitational-wave spectroscopy of massive black holes with the space interferometer lisa. Physical Review D, 73(6), March 2006. ISSN 1550-2368. doi: 10.1103/physrevd.73.064030. URL http://dx.doi.org/10.1103/PhysRevD.73.064030.

[104] Vijay Varma, Maximiliano Isi, and Sylvia Biscoveanu. Extracting the gravitational recoil from black hole merger signals. Phys. Rev. Lett., 124:101104, Mar 2020. doi: 10.1103/PhysRevLett.124.101104. URL https://link.aps.org/doi/10.1103/PhysRevLett.124.101104.

[105] James Healy, Carlos O. Lousto, Ian Ruchlin, and Yosef Zlochower. Evolutions of unequal mass, highly spinning black hole binaries. Phys. Rev. D, 97:104026, May 2018. doi: 10.1103/PhysRevD.97.104026. URL https://link.aps.org/doi/10.1103/PhysRevD.97.104026.

[106] Frank Herrmann, Ian Hinder, Deirdre Shoemaker, Pablo Laguna, and Richard A. Matzner. Gravitational recoil from spinning binary black hole mergers. The Astrophysical Journal, 661(1):430, may 2007. doi: 10.1086/513603. URL https://doi.org/10.1086/513603.

[107] Michael Koppitz, Denis Pollney, Christian Reisswig, Luciano Rezzolla, Jonathan Thornburg, Peter Diener, and Erik Schnetter. Recoil velocities from equal-mass binary-black-hole mergers. Phys. Rev. Lett., 99:041102, Jul 2007. doi: 10.1103/PhysRevLett.99.041102. URL https://link.aps.org/doi/10.1103/PhysRevLett.99.041102.

[108] Alejandro Torres-Orjuela, Xian Chen, Zhoujian Cao, Pau Amaro-Seoane, and Peng Peng. Detecting the beaming effect of gravitational waves. Physical Review D, 100 (6), September 2019. ISSN 2470-0029. doi: 10.1103/physrevd.100.063012. URL http://dx.doi.org/10.1103/PhysRevD.100.063012.

[109] B.P. Abbott et al. Tests of general relativity with gw150914. Physical Review Letters, 116(22), May 2016. ISSN 1079-7114. doi: 10.1103/physrevlett.116.221101. URL http://dx.doi.org/10.1103/PhysRevLett.116.221101.

[110] Reinhard Prix. Bayesian qnm search on gw150914. LIGO Technical Report LIGO-T1500618-v4, LIGO Scientific Collaboration, 2016. URL https://dcc.ligo.org/LIGO-T1500618/public.

[111] Miriam Cabero, Collin D. Capano, Ofek Fischer-Birnholtz, Badri Krishnan, Alex B. Nielsen, Alexander H. Nitz, and Christopher M. Biwer. Observational tests of the black hole area increase law. Physical Review D, 97(12), June 2018. ISSN 2470-0029. doi: 10.1103/physrevd.97.124069. URL http://dx.doi.org/10.1103/PhysRevD.97.124069.

[112] Juan Calderón Bustillo, Paul D. Lasky, and Eric Thrane. Black-hole spectroscopy, the no-hair theorem, and gw150914: Kerr versus occam. Physical Review D, 103 (2), January 2021. ISSN 2470-0029. doi: 10.1103/physrevd.103.024041. URL http://dx.doi.org/10.1103/PhysRevD.103.024041.

[113] Maximiliano Isi and Will M. Farr. Analyzing black-hole ringdowns, 2021. URL https://arxiv.org/abs/2107.05609.

[114] Barak Zackay, Tejaswi Venumadhav, Javier Roulet, Liang Dai, and Matias Zaldarriaga. Detecting gravitational waves in data with non-stationary and non-gaussian noise. Physical Review D, 104(6), September 2021. ISSN 2470-0029. doi: 10.1103/physrevd.104.063034. URL http://dx.doi.org/10.1103/PhysRevD.104.063034.

[115] Collin D. Capano, Miriam Cabero, Julian Westerweck, Jahed Abedi, Shilpa Kastha, Alexander H. Nitz, Yi-Fan Wang, Alex B. Nielsen, and Badri Krishnan. Multimode quasinormal spectrum from a perturbed black hole. Physical Review Letters, 131 (22), November 2023. ISSN 1079-7114. doi: 10.1103/physrevlett.131.221402. URL http://dx.doi.org/10.1103/PhysRevLett.131.221402.

[116] Yi-Fan Wang, Collin D. Capano, Jahed Abedi, Shilpa Kastha, Badri Krishnan, Alex B. Nielsen, Alexander H. Nitz, and Julian Westerweck. Gating-and-inpainting perspective on gw150914 ringdown overtone: Understanding the data analysis systematics. Phys. Rev. D, 112:083023, Oct 2025. doi: 10.1103/3gqn-297f. URL https://link.aps.org/doi/10.1103/3gqn-297f.

[117] Keefe Mitman, Isabella Pretto, Harrison Siegel, Mark A. Scheel, Saul A. Teukolsky, Michael Boyle, Nils Deppe, Lawrence E. Kidder, Jordan Moxon, Kyle C. Nelli, William Throwe, and Nils L. Vu. Probing the ringdown perturbation in binary black hole coalescences with an improved quasi-normal mode extraction algorithm, 2025. URL https://arxiv.org/abs/2503.09678.

[118] Kei ichiro Kubota and Hayato Motohashi. Resonance in black hole ringdown: Benchmarking quasinormal mode excitation and extraction, 2025. URL https://arxiv.org/abs/2509.06411.

[119] Emanuele Berti and Vitor Cardoso. Quasinormal ringing of kerr black holes: The excitation factors. Physical Review D—Particles, Fields, Gravitation, and Cosmology, 74(10):104020, 2006.

[120] Zhongyang Zhang, Emanuele Berti, and Vitor Cardoso. Quasinormal ringing of kerr black holes. ii. excitation by particles falling<? format?> radially with arbitrary energy. Physical Review D—Particles, Fields, Gravitation, and Cosmology, 88(4): 044018, 2013.

[121] Naritaka Oshita. Ease of excitation of black hole ringing: Quantifying the importance of overtones by the excitation factors. Phys. Rev. D, 104:124032, Dec 2021. doi: 10.1103/PhysRevD.104.124032. URL https://link.aps.org/doi/10.1103/PhysRevD.104.124032.

[122] Nils Andersson. Excitation of schwarzschild black-hole quasinormal modes. Phys. Rev. D, 51:353–363, Jan 1995. doi: 10.1103/PhysRevD.51.353. URL https://link.aps.org/doi/10.1103/PhysRevD.51.353.

[123] Nils Andersson. Evolving test fields in a black-hole geometry. Phys. Rev. D, 55: 468–479, Jan 1997. doi: 10.1103/PhysRevD.55.468. URL https://link.aps.org/doi/10.1103/PhysRevD.55.468.

[124] Akash K. Mishra, Gregorio Carullo, and Sumanta Chakraborty. Bounds on tidal charges from gravitational wave ringdown observations. Physical Review D, 109 (2), January 2024. ISSN 2470-0029. doi: 10.1103/physrevd.109.024025. URL http://dx.doi.org/10.1103/PhysRevD.109.024025.